Glomerular Elasticity and Gene Expression Patterns Define Two Phases of Alport Nephropathy

Joonho Yoon*[1], Zhenan Liu*[1], Mathew Alaba*[2], Leslie A. Bruggeman[3], Paul A. Janmey[4], Carlos A. Arana[5], Oluwatoyosi Ayenuyo[6], Isabela Medeiros[6], Sean Eddy[2], Matthias Kretzler[2], Joel M. Henderson[6], Viji Nair[2], Abhijit S. Naik[$#2], Audrey N. Chang[$1,7], R. Tyler Miller[$#1,7,8]

[1]Department of Internal Medicine, University of Texas Southwestern Medical Center, Dallas, Texas, USA

[2]Department of Internal Medicine, University of Michigan, Ann Arbor, Michigan, USA.

[3]Department of Inflammation & Immunity, Lerner Research Institute, Cleveland Clinic, Cleveland, Ohio, USA

[4]Department of Physiology and Institute for Medicine and Engineering, University of Pennsylvania, Philadelphia, PA, 19104, USA.

[5]Department of Immunology, The University of Texas Southwestern Medical Center, Dallas, Texas, 75390, USA

[6]Department of Pathology and Laboratory Medicine, Boston University Chobanian & Avedisian School of Medicine and Boston Medical Center, Boston, MA, USA

[7]Pak Center for Mineral Metabolism and Clinical Research, UTSW Medical Center, Dallas Texas, USA

[8]Medicine Service, VA North Texas Health Care System, Dallas, TX, USA.

[#]Corresponding authors- R. Tyler Miller, UT. Southwestern Nephrology, 8856, 5323 Harry Hines Blvd, Dallas TX 75390, 214-648-7214, tyler.miller@utsouthwestern.edu. Abhijit S. Naik, Nephrology, University of Michigan, Department of Internal Medicine, Division of Nephrology, 1500 E Medical Center Dr, Fl 1, Ann Arbor, MI 48109 abhinaik@med.umich.edu

The authors have declared that no conflict of interest exists.

[1]*Co-first authors. [$]Co-senior authors. These authors contributed equally to this work.

Abstract.

To understand the early stages of Alport nephropathy, we characterize the structural, functional, and biophysical properties of glomerular capillaries and podocytes in *Col4α3*$^{-/-}$ mice, analyze kidney cortex transcriptional profiles over time, and investigate the effects of the ER stress mitigation by TUDCA. We use human FSGS-associated genes (NEPTUNE) to identify common molecular pathways rescued by TUDCA in human glomerular disease and the Alport mouse model. In *Col4α3*$^{-/-}$ mice, podocyte injury is evident by 3 months, with 40% podocyte loss and maximum deformability of glomeruli at 4 months, followed from months 4 to 7 by progressive capillary stiffening, increasing proteinuria, reduced renal function, inflammatory infiltrates, and fibrosis. Evidence of ER stress progresses over this timeframe. Glomerular and renal disease in *Col4α3*$^{-/-}$ mice are suppressed by TUDCA. RNA sequencing at 2, 4, and 7 months reveals an injury-associated gene expression pattern shared by FSGS patients. Deconvolution analysis identified podocyte-associated FSGS gene set that when projected onto 4-month *Col4α3*$^{-/-}$ mouse data was characteristic of hypertrophy, differentiation, and cytoskeleton/adhesion signals. Disease-associated changes in RNAs suppressed by TUDCA in *Col4α3*$^{-/-}$ mice. We define two phases of *Col4α3*$^{-/-}$ nephropathy. The first is characterized by podocytopathy and accelerated podocyte loss, while the second is marked by increased capillary wall stiffening, activation of renal inflammatory and profibrotic pathways, and loss of renal function. Characterization of the effects of TUDCA on *Col4α3*$^{-/-}$ -induced glomerular and renal gene expression and the relation of these genes to human data identifies potential therapeutic targets in Alport and related nephropathies.

Introduction.

Alport nephropathy, caused by COL4A3,4,5 mutations, and other glomerular diseases, including Focal Sclerosing Glomerulonephritis (FSGS), and Minimal Change Disease (MCD), begin with podocyte injury that is followed by varying degrees of proteinuria, hematuria, and tubulo-interstitial damage. The first evidence of podocyte injury is disruption of foot process architecture, foot process effacement, with their flattening, spreading, and loss of slit diaphragms. Further injury leads to detachment, loss of podocytes in the urine, and at some point, irreversible glomerular damage associated with tubulo-interstitial fibrosis and progression to End Stage Renal Disease (ESRD). The mechanisms that cause early podocyte injury in Alport nephropathy and the related transcriptomic changes are not fully defined, although processes responsible for CKD progression, focusing on tubulo-interstitial fibrosis, are increasingly understood.

Podocytes' unique cytoskeletal structure allows them to accommodate traction and shear forces to produce a specific biophysical environment for glomerular capillaries(1-4). Podocyte structure and function are maintained by factors including attachment to the Glomerular Basement Membrane (GBM), lateral attachment of foot processes to foot processes of neighboring podocytes, $Ca+^{2}$ fluxes, various signaling pathways, and mechanical environment (elasticity of the GBM, shear forces, and stretch) (1, 2, 5-10). In rats, 5/6th renal reduction causes glomerular capillary dilation to prevent increased shear stress(11). In acute and chronic glomerular injury models, including Alport nephropathy, protamine, HIV nephropathy, ischemia and ischemia-reperfusion injury, the deformability of glomerular capillaries increases as a result of podocyte injury(1, 2, 12-14). Intravital imaging studies show distension of glomerular capillaries and aneurysms in glomeruli from *Col4αa5*$^{-/-}$ mice at an early stage of disease, indicating increased deformability and reduced structural integrity of these capillaries at a time of accelerated podocyte loss(15-17).

The Alport GBM could injure podocytes through abnormal physical properties or abnormal signaling due to chemical differences in the Alport compared to the normal GBM(8, 18). Alternatively, podocytes that produce COL4α3, 4, and 5 could be injured by accumulation of mutant misfolded collagen molecules with activation of the unfolded protein response (UPR, ER stress) and additional cell-specific remodeling pathways(19-22). Finally, abnormal glomerular capillary mechanics caused by disordered cytoskeletal structure could contribute

to progressive podocyte injury through increased susceptibility to mechanical injury. To begin to distinguish among and refine these injury mechanisms, we treated one group of *Col4α3*$^{-/-}$ mice with TauroUrsoDeoxyCholic Acid (3α,7β-Dihydroxy-5β-cholanoyltaurine, TUDCA), a compound that functions as a chemical chaperone and that protects cells from UPR/ER stress-mediated injury or death(23-26). We analyzed renal function, glomerular capillary elasticity, structure, and renal RNA expression over the eight months of disease and related the transcriptomic data to human NEPTUNE databases.

Results.

Increased glomerular capillary deformability precedes proteinuria and increased creatinine in *Col4α3*$^{-/-}$ mice. We studied the *Col4α3* mutant in the C57/Bl6 background to characterize the progression of Alport nephropathy over the course of the disease. We measured SCr (SCr) (**Figure 1A**) and urine Albumin/Creatinine Ratio (ACR) (**Figure 1B**) beginning at 2 months of age. From 4 months, SCr increased but did not reach statistical significance until 6 months, with a maximum value of 61 μM at 8 months. Similarly, urine ACR increased from 0.82 at 3 months and 3.51 at 4 months to 122 at 8 months, but did not reach statistical significance until 6 months. The SCr and urine ACR values in the control mice remained unchanged significantly over 8 months.

Previous work using kidney disease models demonstrated that glomerular capillary elasticity is linked to podocyte cytoskeletal structure, and that with podocyte injury, capillaries exhibit increased deformability(1, 2, 12, 14). We measured glomerular elasticity, Young's modulus (E), in the control and *Col4α3*$^{-/-}$ mice from 2 to 8 months of age using micro-indentation (**Figure 1C**)(27). The values for E for both the control and *Col4a3*$^{-/-}$ mice were identical at 2 months (2.2 ± 0.2 kPa), and the values for the control mice remained essentially unchanged through 8 months. However, in the *Col4α3*$^{-/-}$ mice, the glomerular E values began to decrease at 3 months (1.85±0.09 kPa) and reached a minimum (1.56 ± 0.3 kPa) at 4 months of age. E then increased to values significantly greater than control by 7 months, reaching a maximum at 8 months (2.7 ± 0.1 kPa). These directionally opposite changes in elasticity early and late in disease signify distinctly different structural and functional properties of glomerular capillaries over time(1-4). The early time point at which reduced glomerular E appears, before significant increases in SCr or urine ACR, indicates that podocyte injury begins early in the course of renal disease and is sufficiently severe to affect overall glomerular capillary mechanical properties.

To understand the molecular processes or pathways activated or inactivated in this Alport model, we performed bulk RNA sequencing of kidney cortical mRNA at 2, 4, and 7 months of age. We identified 2 Differentially Expressed Genes (DEGs) in the 2-month, 1346 DEGs in the 4-month, and 10,475 DEGs in the 7-month WT - *Col4α3*$^{-/-}$ comparisons. The heatmaps shown in **Figure 1D and Figure S1** display the expression of selected genes, grouped vertically by function, from 2 to 7 months. From 2 to 4 months, gene cluster expression patterns

remain relatively stable, reflecting minimal changes in renal function and histology (see below). However, at 2 months, two proximal tubule injury markers, *Lcn2* and *Havcr1*, are upregulated, and remain so with their greatest increases at 7 months. At 4 Mo, corresponding to the nadir of glomerular E, when negligible tubulo-interstitial disease is evident histologically and before the onset of significant proteinuria, increased expression of collagen/fibrosis and inflammation-associated genes, including *Col1α1, Col1α2, Col3α1*, and *Lox* (Lysyl oxidase), *C3, Cxcl1*, *Ccl2, Sox4, Sox9, and Vim* begin in a pattern consistent with altered adaptive/successful repair(28). *Egf*, a marker of tubule health, decreases only at 7 months, a time point at which Pck1, Fbp1, and multiple tubule transporters, including *Slc2a5* (Glut 5)*, Slc26a4* (Pendrin)*, Slc22a7* (OAT2)*, Aqp4, Slc16a4* (monocarboxylic acid transporter), and *Slc12a3* (NCC), are also downregulated demonstrating loss of differentiated tubule metabolic and transport functions. Additionally, markers consistent with maladaptive/failed tubule repair increase de novo or beyond their 4 Mo levels including Ccl2, Ccn2, Cxcl12, Havcr1, Nf-kB, RelB, Runx1, IL-1b, TGF-b, Vcam1, Sox4 and Sox9, and HNF4a decreases(28-30).

In addition to focusing on the set of selected genes above, we performed an unbiased analysis of bulk RNA-seq data. We set a threshold of $|x| \geq 0.5$ to allow only highly relevant biological pathways and minimize statistical noise. All genes had an adjusted p-value of <0.5. The Gene Ontology 2025 tool, which tests biological pathways, cellular processes, and molecular functions enriched within the input gene set, was used. At 4 months, a total of 796 upregulated and 12 downregulated genes met this threshold. Some of the top upregulated pathways included extracellular matrix (ECM), collagen fibril organization, and increased cell matrix adhesion. Increased responses to injury were reflected by genes associated with wound healing, EMT, and inflammatory responses characterized by upregulated activity of phagocytes and cytokine receptor-mediated signaling (**Figure S2, left panel**). The increased expression of cell-type-specific markers for podocytes, such as *Nphs1, Nphs2, and Synpo,* was consistent with increased podocyte differentiation and hypertrophy. Increased expression of genes associated with Hippo-YAP-TAZ signaling (e.g, *Tead3*) provides evidence of increased podocyte differentiation and an ongoing compensatory response to podocyte injury and loss. The top-downregulated pathways, based on the 12 downregulated genes, are those associated with the synthesis of basement membrane components and angiogenesis.

Podocytes are only 1% of the total cells in the kidney, so the molecular signals from other cells in biopsies and bulk RNAseq can overwhelm podocyte gene expression profiles. To obtain a precise podocyte response signal, we employed an approach utilizing biopsy data from 77 NEPTUNE patients with a primary diagnosis of focal segmental glomerulosclerosis (FSGS) who underwent single-nucleus RNA sequencing. Micro-dissected bulk RNA-seq data of 234 glomerular profiles from NEPTUNE patients provided bulk RNA-seq data(31). The microdissected glomerular profiles from NEPTUNE patients underwent independent cluster analysis (ICA), resulting in the identification of a podocyte-enriched gene module comprising 327 genes. We then projected these 327 podocyte-enriched genes onto bulk RNA-seq data from all the mice, identifying a total of 291 mouse orthologs **(Figure S3A)**.

We then deconvoluted the 4-month mouse bulk RNA-seq data to obtain a more podocyte-specific gene set and compared differential gene expression profiles of *Col4α3*$^{-/-}$ with WT mice(31). A total of 60 genes were identified as differentially expressed. Using the same filtering threshold of $|x| \geq 0.5$, a total of 50 genes were identified, 47 of which were upregulated and 3 were downregulated. Similar to the bulk RNA-seq data, the top upregulated processes included podocyte differentiation, EMT, and inflammation (**Figure S3B**). The inflammatory responses were characterized by increased macrophage recruitment, consistent with the bulk data, and cellular responses to chemokines. Other upregulated pathways involve those related to podocyte cytoskeleton, including regulation of the actomyosin structural complex, stress fiber assembly, and filamin binding (**Figure S2, right panel)**. The 3 downregulated genes were those related to angiogenesis and the basement membrane. The bulk RNA-seq data and the deconvoluted RNA-seq data thus complement each other. The bulk data provide richness to the transcriptional profile of all cells, while our deconvolution strategies identify several pathways known to be associated with podocytes, thereby provide more specificity.

,mong the 5364 genes upregulated in the 7-month bulk data, the upregulated biological processes included ECM- and collagen matrix organization (**Figure S4, left panel).** Like the 4-month data, several pathways related to the cellular cytoskeleton and adhesion were upregulated. These included cell-substrate junctions, cell-matrix adhesion, focal adhesions, actin, and filamin binding. Notably, there was increased cytokine production, as well as cytokine and chemokine activity, suggestive of a pro-inflammatory response. Cellular proliferative pathways

were activated. The input gene set was also enriched in pathways annotated for cellular proliferative response in macrophages, lymphocytes, both T and B cells, leukocytes, smooth muscle and dendritic cells. A similar response was noted in pathways related to cell migration. Consistent with the upregulation of pathways related to cytoskeletal reorganization and cellular migration, the activity of GTPase regulators was also upregulated. The overall gene expression pattern was also consistent with activation of the Jak-STAT pathway, PI3K-Akt and MAPK signaling. Of the 1119 downregulated genes, the top downregulated biological processes include oxidative phosphorylation, amino acid catabolic process, fatty acid beta oxidation, branched-chain amino acid processes, sodium ion transport, and the TCA cycle (**Figure S5, left panel**).

We deconvoluted 7-month bulk RNA-seq data using the set of podocyte-enriched genes. Differential gene expression analysis of podocyte-enriched genes from 7-month-old *Col4α3*$^{-/-}$ mice compared to wild-type (WT) mice identified 168 differentially expressed genes (DEGs) with 117 upregulated and 29 downregulated genes that met the thresholding criteria. Upregulated biological pathways were primarily associated with regulation of cytoskeletal dynamics, including cytoskeletal organization, stress fiber assembly, and actin-based movement, alongside processes linked to cellular differentiation and signaling, such as kidney development, regulation of epithelial-to-mesenchymal transition (EMT), neuron projection guidance, Wnt signaling pathway, and regulation of vascular endothelial growth factor (VEGF) production. Inflammatory responses were also enriched, involving the production of cytokines and chemokines (**Figure S4, right panel**). Additionally, pathways related to Golgi lumen functioning, which is associated with protein and lipid modification in the endoplasmic reticulum (ER) were upregulated. Downregulated pathways (**Figure S5, right panel**) included processes related to cell proliferation and signaling, such as regulation of cell population proliferation, regulation of VEGF signaling, and fibroblast growth factor receptor signaling, as well as the interesting finding of sensory perception of mechanical stimuli. Based on the transcriptomic data, there was also evidence of increased apoptosis and podocyte dedifferentiation as noted by reduced *Nphs1* expression. Lastly, the podocin (*Nphs2*) to nephrin (*Nphs1*) ratio (PNR) was elevated (2.45 vs. 1.37, $p<0.05$). An increased PNR reflects podocyte hypertrophic stress in studies of podocyte depletion and is linked to increased urinary podocyte detachment rates, proteinuria, and eventual kidney failure(32).

Taken together, the unbiased analysis of bulk and deconvoluted RNA-seq data from NEPTUNE patients and Col4α3$^{-/-}$ mice, both 4-month and 7-month datasets, revealed upregulated pathways in podocytes linked to ECM organization, collagen fibril formation, cell-matrix adhesion, podocyte differentiation, hypertrophy, EMT, and inflammatory responses, including macrophage recruitment and cytokine-mediated signaling. At 4 months, significant changes were observed in the podocyte cytoskeleton, actomyosin structure, and stress fiber assembly, while downregulated pathways involved angiogenesis and the synthesis of the basement membrane. In contrast, the 7-month data showed a more pronounced inflammatory and proliferative response, with enhanced cytokine production, GTPase activity, and pathways such as MAPK, Jak-STAT, PI3K-Akt, and Wnt signaling. Downregulated pathways at 7 months extended to oxidative phosphorylation and amino acid catabolism, indicating a broader metabolic reprogramming and signaling suppression. Thus, the podocyte-enriched gene sets provided greater specificity for podocyte signals, while bulk RNA-seq captured the broader cortical transcriptional profile.

Correspondence between human and mouse inflammation-related gene expression patterns. Given the observed increase in inflammatory signaling and increased *Tnf* expression by 7 months, we tested whether *Col4α3*$^{-/-}$ mice showed a progressive increase in Tnf-mediated signaling compared to WT mice. For this purpose, we leveraged the study by Mariani et al., which showed increased expression of TNF-α signaling pathway genes in patients with FSGS and MCD associated with poor outcomes. They defined a TNF activation gene signature (272 genes) and an activation score(33). We used this gene signature to assess Tnf activity in our mice at all time points, and identified 205 mouse orthologs that matched the human TNF signature. **Figure 2** shows heatmaps depicting the 50 most upregulated and 50 most downregulated genes in the TNF signature at 2, 4, and 7 months in *Col4α3*$^{-/-}$ mice compared to WT, and shows a heatmap representing the activation score at each time point based on analysis of each mouse and calculation of a Z score. The activation score at 7 months in *Col4α3*$^{-/-}$ mice is significantly different from that of 7-month WT mice and *Col4α3*$^{-/-}$ mice at 2 and 4 months. However, the scores comparing 4 month *Col4α3*$^{-/-}$ to WT at 4 months and *Col4α3*$^{-/-}$ at 2 months are not significantly different, and the WT-*Col4α3*$^{-/-}$ difference at 2 months is not significant. *Tnf*, like many other

inflammation-associated genes, was not differentially expressed at 2 and 4 months (**Supplementary Tables 1A, B**). These data indicate that not only does the Alport nephropathy mouse model express genes associated with proteinuria and poor outcomes in human renal biopsies of patients with glomerular disease, but also show an overlap in inflammatory signaling between human and mouse datasets. Furthermore, in the *Col4α3*$^{-/-}$ mice, the magnitude of the change correlates with the stage of the disease.

Evidence for unfolded protein pathway activation in *Col4α3*$^{-/-}$ podocytes. Podocytes provide mechanical support for glomerular capillaries, determine their elastic properties, form the slit diaphragms, and produce and secrete the Col4α3,4,5 heterotrimer for the GBM(34). Loss-of-function mutations in any one of these collagen chains cause reduced or failed heterotrimer secretion, leading to activation of the UPR in podocytes(22, 32, 35). The mutation in *Col4α3*$^{-/-}$ mice is deletion of the Col4α3 NC1 domain, which should be a severe mutation because post-translational folding is initiated at the NC1 domain (36-38). Cells compensate for excess or misfolded protein by upregulating pathways that improve folding and/or protein degradation, and reduce translation. We imaged WT and *Col4α3*$^{-/-}$ mouse cortex with confocal microscopy and found increased Bip (Hspa5) expression in glomerular podocytes (**Figure 3A**). The levels of Bip and Xbp1s, protein and mRNA, are increased in conditionally immortalized *Col4α3*$^{-/-}$ podocytes compared to their WT counterparts (**Figure 3B**). WT cultured podocytes increase the expression of Bip, Xbp1s, and Ddit3 (CHOP, pro-apoptotic), in response to Tunicamycin, an agent that induces UPR, and the expression is reduced in a dose-dependent manner by treatment with the chemical chaperone, TUDCA (23, 24, 26) (**Figure 3D**). Three genes related to UPR activation were differentially expressed in the *Col4α3*$^{-/-}$ - *Col4α3*$^{-/-}$-T comparison: *Xbp1* (increased 1.85 X), *Dnajb9* (increased 1.52 X), and *Eef1akmt3* (decreased to 0.38 X). For these reasons and the expanded ER in *Col4α3-/-* glomerular podocytes (**Figure S6**), we conclude that an early step in podocyte injury is UPR activation, with disruption of normal protein processing(19, 20, 22). If the effects of UPR activation and podocyte remodeling could be suppressed, podocyte injury could be less severe or develop more slowly.

Bulk-RNA-seq transcriptomic analysis over time showed a progressive activation of the unfolded protein response (UPR) during endoplasmic reticulum (ER) stress. At 4 months, *Atf3* was significantly expressed, indicating early activation of the UPR through the PERK pathway. At the same time, genes like *Srebf1*, *Traf2*,

and *Nfkb2* indicated IRE1-mediated stress signaling, immune responses, and activation of MAPK pathways. By 7 months, a distinct UPR signature developed. Genes including *Atf3, Atf6, Atf6b, Ddit3, Eif2ak3, Ern1, Hspa5, and Xbp1* were upregulated, encoding key UPR transducers like IRE1α, PERK, and ATF6, and effectors such as BiP and XBP1s. This pattern reflects increasing ER stress adaptation, including translational attenuation, chaperone induction, and ER-associated degradation. Overall, the results show a gradual escalation of proteotoxic stress response from 4 to 7 months.

TUDCA treatment slows progression of renal disease in *Col4α3$^{-/-}$* mice. We investigated the role of ER stress in kidney disease in Alport mice by feeding *Col4α3$^{-/-}$* mice TUDCA incorporated into mouse chow (0.8%) from the time of weaning, 21 - 25 days old, through the end of studies and comparing physiologic, morphologic, and transcriptomic changes among WT, *Col4α3$^{-/-}$*, and TUDCA-treated *Col4α3$^{-/-}$* mice((39). WT littermates served as controls. We measured the effects of TUDCA treatment on *Col4α3$^{-/-}$* mouse SCr (**Figure 4A**), urine ACR (**Figure 4B**), and E, the elastic modulus of glomeruli (**Figure 4C**) at 4 and 7 months, the nadir and peak of glomerular E (**Figure 1C**). At 4 months, SCr and urine ACR values were similar among the WT, *Col4α3$^{-/-}$*, and TUDCA-treated *Col4α3$^{-/-}$* (*Col4α3$^{-/-}$*-T) groups (**Figure 4**, left top two panels). However, at 7 months, average ACR and SCr values were respectively 90±11 and 55±7 μm in the Col4α3$^{-/-}$ mice; values for SCr and ACR in the Col4α3$^{-/-}$-T mice were 40±8.6 and 33±3.9 μm. At 4 months, the value for E in the WT mice was 2.1±0.04 kPa, 1.56±0.05 kPa for the *Col4α3$^{-/-}$* mice, and 2.0±1.0 kPa in the *Col4α3$^{-/-}$*-T mice (**Figure 4C**). At 7 months, WT glomerular E was 2.1±0.06 kPa, and for the *Col4α3$^{-/-}$* glomeruli it was 2.70±0.05 kPa, while the value for the *Col4α3$^{-/-}$*-T glomeruli was 1.9±0.04 kPa, a value comparable to WT.

TUDCA treatment preserves *Col4α3$^{-/-}$* kidney structure. Chronic kidney disease is marked by progressive fibrosis and loss of renal function, a component of which can be attributed to proteinuria(40). Our physiologic measurements at 7 months, late-stage disease (**Figure 4A-C**), showed preserved renal function in the *Col4α3$^{-/-}$*-T mice, implying preserved glomerular and renal structure. Low magnification kidney sections from 4-month mouse kidneys stained with PAS or Picrosirius Red (PSR) show that sections from WT, *Col4α3$^{-/-}$*, and *Col4α3$^{-/-}$*-T mice are indistinguishable (**Figure S8**), indicating that at the 4-month time point, overall renal parenchymal injury is minimal. At seven months (**Figure 4D**), the extent of injury in the Col4α3$^{-/-}$ kidneys is evident in the PAS

and PSR-stained sections. Compared to the control kidneys, the PAS-stained *Col4α3*$^{-/-}$ kidneys show fibrosis, inflammatory cell infiltrates, and disrupted renal architecture. In the kidneys of *Col4α3*$^{-/-}$-T mice, these features are present, but to a significantly lesser extent. The insets show representative images of glomeruli from each group. The glomeruli from the *Col4α3*$^{-/-}$ mice are sclerotic and have excess, irregular PSR staining. Although glomeruli from the *Col4α3*$^{-/-}$-T mice are not normal, their structure is relatively preserved compared to the untreated *Col4α3*$^{-/-}$ glomeruli.

Expression of genes associated with renal injury and fibrosis at 7 months was measured using qRT-PCR and showed normalization by TUDCA in *Col4α3*$^{-/-}$ mice (**Table 1**). Expression of *Col1α1, Col1α2, Col3α1*, lysyl oxidase (*Lox*), lysyl oxidase-like 2 (*Loxyl2*), *Tgfb1*, *Cxcl1, Ccl2, Ccr2*, *Cn1* (Cyr61), a gene involved in development and wound healing and repair, *Tnf*, and *Igf2*, a gene involved in hypertrophy, all increased in *Col4α3*$^{-/-}$ mice compared to WT. In the *Col4α3*$^{-/-}$-T mice, the mRNA expression for these genes was reduced to levels intermediate between those in WT and untreated *Col4α3*$^{-/-}$ mice. *Egf* mRNA, a marker for renal tubular health, decreased significantly (20% vs WT) in the *Col4α3*$^{-/-}$ mice compared to Control, but in *Col4α3*$^{-/-}$-T mice, *Egf* mRNA was expressed at an intermediate level (70% of WT). TUDCA, initiated early in the disease, reduces proteinuria, glomerular injury, and renal parenchymal injury. TUDCA slows the progression of nephropathy in *Col4α3-/-* mice, in part, by reducing cytokine and chemokine production and fibrosis.

TUDCA reduces podocyte loss from *Col4α3*$^{-/-}$ mouse glomeruli. Glomerular capillaries become deformable at 3 months, before significant increases in SCr or urine ACR, indicating that podocyte injury begins at or before that time. Alport patients lose podocytes in the urine at an accelerated rate, and podocytes can be detected in their urine before significant proteinuria develops(16, 17)**.** We compared glomerular podocyte density in WT, *Col4α3*$^{-/-}$, and *Col4α3*$^{-/-}$-T mice at 2, 3, and 4 months using WT1 staining as a podocyte marker (**Figure 5**)(41). At 2 months, before the reduction of glomerular E in the *Col4α3*$^{-/-}$ mice, the podocyte density was similar among all three groups. At 3 months, when increased deformability was detectable in the *Col4α3*$^{-/-}$ glomeruli, podocyte density remained unchanged in the three groups and was comparable to the values for 2-month WT glomeruli. In the 3-month *Col4α3*$^{-/-}$ mice, the SCr and ACR values were similar to those for the WT mice. However, at 4

months, podocyte density was reduced by 40% in the *Col4α3-/-* glomeruli, and TUDCA treatment protected the glomeruli from podocyte loss.

Early glomerular capillary deformability corresponds to reduced podocyte adhesion. Based on the 40% reduction in podocyte density in the 4-month *Col4α3*$^{-/-}$ mice (**Figure 5**), we thought that podocyte injury should be detectable at 3 months as decreased podocyte adhesion, because that is the earliest detectable change in capillary elasticity, and *Col4α3*$^{-/-}$ podocyte numbers are preserved. WT and *Col4α3*$^{-/-}$ glomeruli had similar patterns of synaptopodin and nephrin staining, indicating preserved structure at that level (**Figure S8**). To test this possibility, we measured podocyte adhesion in 3-month-old mice as urinary podocyte loss *in vivo* in response to volume loading. Mice were injected with 0.5N saline (80 µl/g IP), and urine was collected over two hours(42). Urinary podocytes were quantified using two methods: immunoblot analysis of urine for nephrin, normalized for creatinine (**Figure 6A, B**), and counting WT-1-positive cells in the urine sediment (**Figure 6C**). With volume loading, the amount of urinary nephrin increased fourfold over WT in the *Col4α3*$^{-/-}$ samples, and TUDCA treatment reduced urine nephrin by approximately half. Urinary podocyte loss increased in *Col4α3*$^{-/-}$ mice compared to WT (**Figure 5C**). These observations were consistent across 3 different experiments, where, although the total number of podocytes lost in the urine varied from mouse to mouse, only the *Col4α3-/-* mice had multiple WT-1-positive cells in their urine. Reduced podocyte adhesion and loss occur early in nephropathy, suggesting that early disease-associated structural alterations in podocytes, including adhesion, may contribute to the increased deformability of glomerular capillaries. TUDCA protects against podocyte loss at this early stage of nephropathy.

TUDCA protects glomerular capillary and podocyte structure. Light microscopic images of glomeruli from 4-month-old *Col4α3*$^{-/-}$ mice show generally preserved structure, but the glomeruli are hypertrophic compared to the WT mice and have multiple dilated capillaries (**Figure 7, top row**). Additionally, focal lesions are present, but there is little evidence of tubulo-interstitial damage. The *Col4α3*$^{-/-}$-T glomeruli show evidence of focal lesions and capillary dilation, but considerably less than the *Col4α3*$^{-/-}$ glomeruli and have no evidence of hypertrophy. At 7 months, the patterns described above persist, but in the *Col4α3*$^{-/-}$ mice, they are more severe, characterized by increased glomerulosclerosis, focal glomerular lesions, and significant tubulo-interstitial injury and

inflammation. The *Col4α3*$^{-/-}$-T kidneys show less glomerular and tubulo-interstitial injury compared to the *Col4α3*$^{-/-}$ kidneys, but injury progressed from the 4-month time point (**Supplemental Table S2).**

We used transmission electron microscopy (TEM) to compare podocyte and GBM structures in our three groups of mice at 4 and 7 months (**Figure 8**). At 4 months, the glomeruli from *Col4α3-/-* mice exhibit regions of irregular GBM structure, characterized by both thin and thick regions. The podocyte foot processes are normal in some regions but also show evidence of effacement and widening in other regions. Some podocyte cell bodies appear hypertrophic, exhibiting vacuolization, and have expanded ER indicative of ER stress, and microvillus formation (**Figure S6, Supplemental Table S3**. In the *Col4α3*$^{-/-}$-T glomeruli, these pathologic findings are present, but less severe than in the Col4α3$^{-/-}$ mice. By 7 months, the pathologic changes in the *Col4α3*$^{-/-}$ GBMs and podocytes are more advanced, with evidence of substantial glomerulosclerosis. The *Col4α3*$^{-/-}$-T glomeruli have characteristics intermediate between the WT and Col4α3$^{-/-}$ glomeruli. The pathologic findings are quantified in **Supplemental Table S5**.

Effect of TUDCA on the transcriptomic profile of 4-month-old Col4α3-/- mice: We assessed the effects of TUDCA on gene expression in 4-month-old Col4α3$^{-/-}$ mice using bulk RNA sequencing, as this age represents a critical transition point in disease progression. Using the same thresholding criteria as earlier, we identified 62 genes to be upregulated (from a total of 128 DEGs). The top enriched biological pathways were those that negatively regulate ERK1/ERK2 (part of the MAPK pathway), peptidyl-tyrosine dephosphorylation, protein phosphorylation, and Phosphatidylinositol 3-Kinase/Protein Kinase B Signal Transduction (PI3K/PKB) (**Figure S9, left pane**l). Genes coding for proteins involved in the mitigation of reactive oxygen species (ROS), *e.g., Gstm, Gstt1, Txnrd3,* were also upregulated. Among the 29 downregulated genes, AMP binding (*Prkag3* - a regulatory subunit of AMPK*)* was the only molecular process that was significantly downregulated. Several other genes were downregulated, including those involved in fatty-acyl-CoA synthesis (*Acsm5*) activity, gluconeogenesis (*Fbp1,* rate limiting step in gluconeogenesis), endopeptidase inhibitor activity (*Timp3, Mansc4*), cell-cell junction (*Igsf11, Pdlim2, Ildr2*) and key genes associated with ECM, such as (*Hapln1, Timp3, Vwa1),* mitigating cellular growth and proliferative responses *(Ccnd1, Egfr)* **(Figure S10, left panel).** These data suggest that overall, at the bulk-RNA seq level, TUDCA works via major effects on signaling and metabolism, reducing

ERK1/ERK2 signaling, promoting anti-apoptotic PI3K/PKB activity, and reducing cellular metabolism, growth, and proliferation, while increasing the generation of ROS-scavenging proteins, accompanied by preservation of phenotype and kidney function.

As noted earlier, at 4 months, 60 genes were differentially expressed between Col4α3$^{-/-}$ mice treated with TUDCA and untreated Col4α3$^{-/-}$ mice. We evaluated the effect of TUDCA on the directionality of these 60 genes to identify altered transcriptomic programs that correspond to preservation of their morphological and functional phenotype (**Figure S11**). The same deconvolution strategy described previously was applied. Col4α3$^{-/-}$ mice treated with TUDCA exhibited a reversal of expression in 26 genes and an increase in expression in 34 genes. To refine our analysis, we restricted enrichment to genes meeting a log2 fold-change threshold of ≥0.1 or ≤-0.1. Using this approach, 14 genes reversed their expression direction, while the expression of 19 genes was increased.

Pathway enrichment analysis of genes reversed with TUDCA revealed suppressed pathways related to podocyte development and differentiation (e.g., *Nphs1* and Nphs2), as well as those involved in growth and extracellular matrix (ECM) organization, all of which were upregulated in the Col4α3$^{-/-}$ disease state (**Figure S9, right panel**). Cellular components reversed included pathways related to the basement membrane, cell-cell junctions, collagen-containing ECM, and rough endoplasmic reticulum. Molecular processes reversed encompassed endopeptidase inhibitor activity, urea transporter activity, Wnt signaling, and alpha- and gamma-tubulin activity. In contrast, TUDCA enhanced pathways associated with actin filament bundle assembly and ECM organization, while reducing cell migration but enhancing cell motility (**Figure S10, right panel**). Pathways related to angiogenesis were also upregulated. Thus, TUDCA shifted disease-associated gene expression patterns toward the WT pattern.

Given that the 60 podocyte-associated genes were hypothesized to be involved in the mechanistic pathway of Alport nephropathy progression, we investigated whether similar effects could be observed in other model systems. We analyzed a dataset from an F1 hybrid Col4a3$^{-/-}$ mouse model (129/SvJ × C57BL/6J) (42), which exhibits accelerated disease progression compared to the Bl6 model (**Figure S12**)(43). These mice were treated with either anti-miR-21 or angiotensin-converting enzyme inhibitors (ACEi), starting at 4 weeks of age when proteinuria was already evident. In contrast, minimal proteinuria was observed in our Alport mice when TUDCA treatment was initiated. The animals were sacrificed at 15 weeks of age for RNA-seq analysis. Using a similar

deconvolution approach, we extracted expression values for the 60 genes we identified from the published bulk RNA-seq data (NEPTUNE) and compared the effects of anti-miR-21 or ACEi to TUDCA treatment(31). In the anti-miR-21-treated group, 49 of the 60 genes were differentially expressed, whereas in the ACEi-treated group, 38 of the 60 genes showed differential expression. In the TUDCA-treated group, none of the genes were differentially expressed compared to the anti-miR-21 and ACEi groups. Despite the absence of statistically significant expression in the TUDCA group, the directional response of mRNA to therapy was highly consistent across all three therapeutic interventions. The weaker response to TUDCA compared to anti-miR-21 and ACEi could be attributed to the advanced disease state (evidenced by proteinuria) already established by 4 weeks in the anti-miR-21 and ACEi-treated groups, and potentially a higher amplitude signal for disease suppression.

Translatomic analysis of Differentially Expressed Genes in 4-month-old Col4a3-/- Mice Mapped to Human Orthologs predicts long-term function in glomerular disease. To assess the relevance of the 60 genes identified in the podocyte-enriched data to human health, we performed Cox regression analysis to examine the association between these genes and clinical outcomes among NEPTUNE patients. Outcomes were defined as the time to end-stage renal disease (ESRD) or a 40% decline in estimated glomerular filtration rate (eGFR) compared to baseline (ESRD40). To address multicollinearity in this high-dimensional dataset and to identify biologically relevant genes, we used a Lasso model, which identified a total of eight genes: *SLC14A2, NKD1, CRB2, GPC6, NPHS1, FOXC1, STX11*, and *FRY*, and found that four, *NKD1, CRB2, GPC6, and STX11* were associated with risk for ESRD40. In a multivariable Cox model adjusted for age, gender and race, a log2-fold increase in the expression of *CRB2* and *GPC6* was associated with hazard ratios (HRs) of 1.62 (95% CI: 1.20–2.20) and 2.62 (95% CI: 1.42–4.80) for the risk of graft failure, respectively. Conversely, a log2-fold reduction in NKD1 expression was associated with an HR of 0.37 (95% CI: 0.15–0.90), and for STX11 a HR of 0.42 (95% CI 0.21 – 0.87) **(Figure S13).**

Discussion.

We followed the course of nephropathy in *Col4α3*$^{-/-}$ mice (C57Bl6 strain) from 2 to 8 months of age to identify mechanisms of renal injury at early time points. We assessed renal function and structure as well as glomerular capillary and podocyte structure, function, elastic properties, and gene expression. We have three principal findings. First, in *Col4α3*$^{-/-}$ mice, Alport nephropathy has two distinct phases. In the first phase, from birth through 4 months, podocyte injury and loss occur in the absence of significant proteinuria, reduced renal function, or tubulo-interstitial injury. Evidence of podocyte injury includes increased deformability of glomerular capillaries, reduced adhesion of podocytes to glomerular capillaries, foot process effacement, and podocyte loss. Increased deformability probably sensitizes the capillaries to mechanical hemodynamic injury, accelerating podocyte loss. The gene expression profile is consistent with increased podocyte hypertrophy, differentiation, motility and proliferative pathways likely in response to podocyte depletion. Additionally, an early inflammatory response is present. This early phase may represent reversible disease. The second phase, from 4 months with approximately 40% podocyte loss, is characterized by increasing glomerulosclerosis, rigidity of glomerular capillaries, progressive proteinuria and tubulo-interstitial fibrosis. The gene expression profile is consistent with podocyte dedifferentiation, increased expression of genes associated with fibrosis and tubular injury, and reduced expression of genes related to renal transport function and tubular health, such as EGF. There is also a marked increase in inflammatory signaling, particularly TNF. This second phase is likely to represent an irreversible phase of the disease.

The second significant finding is that TUDCA, a chemical chaperone that reduces the consequences of UPR activation, significantly slowed the progression of renal disease in *Col4α3*$^{-/-}$ mice by preserving podocyte and glomerular structure, at the earliest time point it was detected, 3 Mo, and resulting in a 50% reduction in SCr, 65% reduction in urine ACR, and near normalization of glomerular capillary E at 7 months. These data and two other recent publications demonstrate that interfering with UPR activation suppresses the Alport renal disease phenotype and implicate the UPR pathway in initial podocyte injury(19, 22).

Third, we identified an early podocyte gene expression profile related to Alport podocytopathy and nephropathy by deconvoluting the four-month mouse bulk RNA-seq data to define a podocyte-enriched gene set based on

single nucleus and bulk RNAseq data from NEPTUNE patients(31). We found a common set of podocyte genes characteristic of early injury in Alport nephropathy in two mouse strains, our TUDCA-treated Bl6 mice and the Sv129 x B6 F1 hybrid mice treated with anti-Mir21 and ACEI(43). Both treatments suppressed the Alport phenotype and caused similar changes in gene expression in their respective mice (**Supplemental Figures S11, 12**). This gene set is also shared with human FSGS patients. Further, we found that four of the TUDCA-responsive genes in the Alport mouse group confer risk for ESRD40 in the FSGS dataset further demonstrating the relevance of the gene set identified in Alport mice to human disease (**Supplemental Figure S13**). These results indicate that the 60-gene set we identified is mechanistically linked to podocyte injury, differentiation, and disease progression in currently available Alport model systems. This gene set probably represents an early pattern of injury common to many diseases but not the initial injury pathway because of the time point, 4 Mo, the disease characteristics of the mice at 4 Mo, and its shared features with human FSGS patients with established disease.

TUDCA treatment prevents glomerular hypertrophy in 4-month *Col4α3*$^{-/-}$ mice. Many of the 60 TUDCA-responsive genes are related to cell growth. Expression of genes associated with differentiation and hypertrophy including *Nphs1, Nphs2, Synpo, Plce1,* and *Cdkn1c*, is increased as is the expression of genes associated with growth, including Fzd2 (Frizzled class 2 receptor, involved in Wnt signaling), Nkd1 (NKD inhibitor of Wnt signaling pathway1), Tead3 (TEA domain transcription factor 3, involved in the Hippo signaling pathway), Srgap2 (Slit-Robo Rho GTPase Activating protein 2) and Foxc1 (Forkhead Box C1) (**Figure 9, Supplemental Figure 11, Supplemental Table 6**). In the TUDCA-treated *Col4α3*$^{-/-}$ mice that do not have hypertrophic glomeruli, the direction of change in these genes is reversed, and the increase is minimized in the remaining two, Nkd1 and Foxc1. The hypertrophy-associated increased expression of these genes, coupled with their suppression in response to TUDCA and the absence of hypertrophy in the treated group, validates the idea that this gene set is part of the causal pathway in the *Col4α3*$^{-/-}$ glomerular disease phenotype. This gene set is relevant to human glomerular disease based on its presence in human disease data. The increased expression of genes such as Edn1, Lox, and Aif1 shows that injury is ongoing.

Podocyte injury, hypertrophy in response to podocyte loss, or other hypertrophic stimuli can cause increased capillary deformability that may be part of a podocyte-specific remodeling program(1, 2, 14, 44-46). The first

observed step in podocyte injury is the rearrangement of podocyte cytoskeletal structures with effacement of foot processes, ultimately leading to cell loss. Hence, a difference between the biophysical properties of effaced or injured and normal podocytes is a reasonable expectation. Increased podocyte and capillary deformability may predispose to hemodynamic mechanical trauma, shear and deformation stresses, accelerating glomerular failure, consistent with the beneficial effect of ACEi/ARB therapy(43, 46, 47). Our finding of increased capillary deformability in the *Col4α3*$^{-/-}$ mouse model is supported by studies of Gyarmati et al, who found dilated glomerular capillaries with aneurysms and thrombi in early-stage Col4α5$^{-/-}$ KO mice (C57/Bl6 background), similar to our results, where capillary deformability was measured directly(15). Podocyte hypertrophy, also present in our *Col4α3*$^{-/-}$ mice, is sufficient to increase the deformability of podocytes and glomerular capillaries (1, 44). In this setting, even normal blood pressure is likely to injure podocytes, and hypertension would be even more damaging(46). Capillary deformability could be a therapeutic target.

Until recently, showing the benefit of UPR suppression on the course of Alport nephropathy in vivo has been difficult(19-22). Several factors may contribute to this situation. First, podocyte injury probably begins with expression of the disrupted *Col4α3,4,5* heterotrimer before or near birth, long before clinical evidence of disease, and accelerates with birth and post-natal renal perfusion(34, 48). Our intervention began at the time of weaning, 4 weeks after birth and at least 12 weeks before significant proteinuria or reduced renal function were evident in the Bl6 model.

Suppose interventions start with the onset of “clinical” evidence of renal disease, 4 – 6 months in the Bl6 model. In that case, sufficient injury is present that renal function may not be stabilized, or its rate of loss not slowed. In models that progress more rapidly, such as the SvJ strain or with severe mutations such as the *Col4α5* G5X mutation, proteinuria and renal failure occur earlier, compressing the course of disease. Interventions would occur later in the disease with more severe preexisting pathology than in our current studies, and the ability to see treatment responses would be limited(37, 49). Conversely, milder mutations, such as those in the collagenous domain that have less severe effects on folding and secretion, may result in later onset or milder disease and be easier to treat.

Yu et al studied the Col4α3 G799R mutation in the Bl6 strain and started TUDCA at 4 months(19). This mutation, located in the collagenous domain, exhibits a milder phenotype compared to Col4α3$^{-/-}$, as it prevents the initiation of heterotrimerization due to a deletion of the Col4α3 NC1 domain. Similarly, Ioannou et al studied the Gly1332Glu collagenous domain mutation in Svj129 mice and found suppression of the Alport phenotype in response to 4PBA. They also showed partial restoration of Col4a3, 4, 5 secretion in cultured primary podocytes by 4BPA, but not TUDCA(22). Rubel et al. initiated ACEI therapy at 4 weeks and anti-miR-21 therapy at 6 weeks, a later stage of disease than in our studies, and found comparable benefit(43). The magnitude and nature of the effect of anti-miR-21 and the synergistic effects of ACEI treatment may be responsible for the success of their approach. Additionally, the effects were more pronounced in the more slowly progressing F1 hybrid Svj126 X Bl6 *Col4α3*$^{-/-}$ mice(42). Gale et al. reported a randomized controlled trial of anti-miR21 in adult Alport patients that was stopped for lack of effect on proteinuria despite preclinical success in mice(50). The patients began treatment with a mean eGFR value of approximately 55 ml/min/1.73 m^2/yr, an eGFR slope of **-**8 ml/min/1.73 m^2/yr, and a mean UACR value of 2681. These patients had kidney disease that was probably equivalent to that in our 6-month mice with established glomerular and parenchymal injury. Advanced disease is less likely to respond to treatment than if treatment had been started earlier.

TUDCA suppresses the effects of UPR activation and, in these studies, preserves glomerular and renal function. Although UPR-mediated injury of podocytes appears to be an early step in Alport nephropathy, podocyte injury probably initiates distinct, later processes in other glomerular cells, such as endothelial cells, that contribute to glomerular injury progression. Thus, with disease progression, each cell type could have its own disease trajectory that interacts with other cells and mediators of inflammation. Following the development of significant proteinuria, the mechanisms of tubulo-interstitial injury are probably shared among many proteinuric diseases (late disease)(38). This scenario suggests targeted therapies to processes such as endothelial injury and fibrosis driven by IL-11, which we see increased at 7 months(15, 51). The beneficial effects of TUDCA may derive from improved podocyte function as suggested by our transcriptomic analysis, but TUDCA may have additional effects, including suppression of inflammation(19, 25, 52, 53). An interesting finding in our 4 Mo bulk RNase data is a strong signal for inhibition of MAPK/ERK signaling by TUDCA (**Fig. S6A**). Three dual specificity phosphatases, Dusp5, 6, and 9 were upregulated 1.6, 1.8, and 1.7-fold respectively by TUDCA. Suppression of

MAPK/ERK signaling could have a beneficial general effect on all kidney cell types in the context of injury and inflammation.

Using our deconvolution strategy, we identified a subset of podocyte genes in bulk RNAseq data of *Col4α3*$^{-/-}$ mice that respond to TUDCA (**Figure 9, Supplemental Figure S11 and Table S6**). This set of TUDCA-responsive genes also responded to treatment with anti-miR-21 and ACEi in the study by Rubel et al. in Svj/129 F1 mice (**Supplemental Figure S14**(43). The similar behavior of these genes in different models of Alport syndrome, their relationship to human glomerular disease, and their response to different interventions suggest that these gene sets not only reflect disease behavior in mouse models of Alport nephropathy but are also relevant to human podocytopathies, including Alport nephropathy and FSGS. This pattern of gene expression may represent an early, but general response to podocyte injury, so that it may have relevance to other diseases, particularly FSGS and IgA Nephropathy with *Col4α3,4,5* mutations and heterozygous states(54, 55). Four of the podocyte-associated TUDCA-responsive genes, *NKD1, CRB2, GPC6,* and *STX11*, were associated with ESRD40 in the NEPTUNE FSGS population demonstrating their relevance to human disease. To the extent that UPR activation is a component of other podocyte and glomerular diseases, these gene sets may be relevant to developing novel therapeutics. Podocyte injury and downstream renal injury could be mitigated by TUDCA or by targeting its downstream signaling pathways if initiated early, before the disease is irreversible. The presence of these injury-associated transcriptomic patterns early in the course of disease, before conventional evidence of renal damage, 3 - 4 Mo in our model, and that can be manipulated therapeutically may identify a phase when disease can be reversed or arrested and supports pursuing earlier diagnosis and treatment for glomerular diseases.

Methods.

Reagents. All fluorescent antibodies were purchased from Invitrogen. *Antibodies for immunofluorescence* **-** Col4α3: (Rat) Clone H31 97076), Chondrex, Inc.; Col4α3: (Rabbit) MBS2026491, BioSource; Bip: ab21685, Abcam; WT-1: sc-7385, Santa Cruz; Synaptopodin: sc-21537, Santa Cruz; Nephrin: AF3169, R&D Systems. *Antibodies for immunoblotting* - Bip: ab21685, Abcam; Xbp1s: sc-7160, Cell signaling, and 24868-1-AP, Proteintech; Chop: (D46F1), #5554, Cell Signaling; GAPDH: XP, #5174S, Cell signaling; β-actin – #AM4302 Invitrogen.

Mouse breeding and treatment. Col4α3$^{-/-}$ mice (C57Bl/6J) were obtained from Jeff Miner(36). Genotyping was performed by Transnetyx. For studies, homozygous males were bred with heterozygous females to obtain Col4α3$^{-/-}$ and Col4α3$^{+/+}$ mice. Col4α3$^{-/-}$ mice were fed 0.8% TauroUrsoDeoxyCholic Acid, 3α,7β-Dihydroxy-5β-cholanoyltaurine (TUDCA) incorporated into mouse chow from the time of weaning (25-28 days old) until sacrifice (23, 24, 26, 37). TUDCA (98% purity) was from Chemimpex and was incorporated into standard mouse chow by Teklad. Normal littermates served as controls.

SCr was measured either by submandibular puncture or exsanguination at the time of sacrifice. After clotting at room temperature for 1 hour and centrifugation at 2000 x g for 10 minutes, the supernatants were transferred to new clean tubes and stored at -80 °C for further analysis. Mouse urine samples were collected from spot urine in clean empty cages and centrifuged at 400 x g for 10min. The supernatant was transferred to new, clean tubes and stored at -80 °C. Urine albumin concentrations were measured using a Mouse Albumin ELISA Kit (Immunology Consultants Laboratory, Inc.). Serum and urine creatinine levels were measured by UTSW O'Brien Kidney Research Center Physiology Core using capillary electrophoresis. Urine albumin-to-creatinine ratios were calculated to assess the severity of albuminuria.

Podocyte adhesion was measured in vivo by injecting 0.5N saline (80 µl/g IP) and collecting urine over two hours(42). An aliquot of urine was normalized for creatinine and immunoblotted for nephrin. Another aliquot was centrifuged, the sediment attached to a slide and stained for DAPI and WT-1.

Isolation of mouse glomeruli. To isolate glomeruli, kidneys were removed from mice, placed in iced buffer, decapsulated, and cortices dissected from medullae on ice, minced, and pushed through a screen (180 µm,

W.S. Tyler Co, Cleveland, OH) with a flexible spatula. The minced tissue was suspended in PBS with 5.5 mM glucose and 0.3 mM pyruvate (GIBCO), filtered through a 90 μm nylon mesh (Falcon) to remove vessels and large pieces of tissue. The filtrate was collected in a 45 μm mesh nylon filter (Falcon) that contained intact glomeruli with minimal tubular contamination (< 2%)(1, 2, 56). Glomeruli were maintained in DMEM with 0.1% FBS at room temperature before elasticity measurements or imaging.

Podocyte cell line development and culture. Podocyte cell lines were derived from WT and Col4α3$^{-/-}$ primary podocyte outgrowths from glomeruli isolated from adult mice (12-16 weeks of age). Glomeruli were maintained in DMEM with 0.1% FBS at room temperature and seeded onto collagen I-coated dishes for 4-6 days to allow cell outgrowth. Primary podocytes were then trypsinized, filtered with a 20 μm cell strainer, and re-plated for experiments or immortalization. Primary podocytes were conditionally immortalized by infection with a lentivirus expressing the temperature-sensitive SV40 T antigen tsA58. Lentivirus was produced from pLenti-SV40-T-tsA58 (abm cat# LV629) as previously described (57) using the VSV envelope from pMD2.G (Addgene cat#12259), and the packaging plasmid pCMV delta R8.2 (Addgene cat # 12263), gifts from Didier Trono. Primary glomerular outgrowths were infected for 48 hours, followed by selection with puromycin (2ug/ml). Conditionally immortalized mouse podocytes were cultured in RPMI 1640 with 10% FBS. Cell cultures were expanded at 33°C and, for experiments, differentiated at 37°C for 7-10 days as previously described(58).

Animal Studies. Animal research was performed in accordance with the UT Southwestern Medical Center Animal IACUC guidelines. The research study protocol (number 2014-0078) was approved by the UT Southwestern Medical Center Animal IACUC (NIH OLAW Assurance Number A3472-01). UT Southwestern Medical Center is fully accredited by the American Association for the Assessment and Accreditation of Laboratory Care, International (AAALAC). Animals are housed and maintained in accordance with the applicable portions of the Animal Welfare Act and the Guide for the Care and Use of Laboratory Animals. Veterinary care is under the direction of a full-time veterinarian boarded by the American College of Laboratory Animal Medicine. Mice were sacrificed for experiments by first anesthetizing with Avertin and then euthanizing by exsanguination.

Kidney total RNA preparation for RNAseq. Kidneys were removed, and 20 mg of cortex was processed for RNA purification. All samples were stored with RNA later at -80 °C and thawed for RNA purification. Total RNA was purified using Direct-Zol™ RNA Miniprep Plus (Zymo Research), and the concentration was measured with

DS-11 FX+ (Denovix). Final RNA samples were submitted for sequencing to the Next Generation Sequencing Core of UTSW. Sequence analysis and results were performed by the University of Michigan Nephrotic Syndrome Study Network (NEPTUNE).

Quantitative RT-PCR. Total RNAs were purified from each group of mouse cortices using Direct-Zol™ RNA Miniprep Plus (Zymo research) and used for reverse transcription by SuperScript III First-Strand Synthesis System (Invitrogen). Quantitative PCR was carried out with specific primers using SYBR™ Green PCR Master Mix (Applied Biosystems) and StepOnePlus™ Real-Time PCR System (Applied Biosystems). For quantitative analysis, the samples were normalized to GAPDH (Glyceraldehyde 3-phosphate dehydrogenase) gene expression using the ΔΔCT value method. Primer sequences for specific genes are below.

C3 forward: 5'-CGCAACGAACAGGTGGAGATCA, reverse: 5'-CTGGAAGTAGCGATTCTTGGCG-3'

Ccl2 forward: 5'-GCTACAAGAGGATCACCAGCAG-3', reverse: 5'-GTCTGGACCCATTCCTTCTTGG-3'

Ccr2 forward: 5'-GCTGTGTTTGCCTCTCTACCAG-3', reverse: 5'-CAAGTAGAGGCAGGATCAGGCT-3'

Cxcl1 forward: 5'-TCCAGAGCTTGAAGGTGTTGCC-3', reverse: 5'-AACCAAGGGAGCTTCAGGGTCA-3'

Col1α1 forward: 5'-GGAGAGAGCATGACCGATGG-3', reverse: 5'-AAGTTCCGGTGTGACTCGTG-3'

Col1α2 forward: 5'-GCTGGTGTAATGGGTCCTCC-3', reverse: 5'-ATCCGATGTTGCCAGCTTCA-3'

Col3α1 forward: 5'-AGGCTGAAGGAAACAGCAA-3', Col3α1 reverse: 5'-TAGTCTCATTGCTTGCGTG-3'

Col4a3 forward: 5'-CAAAGGCATCAGGGGAATAACT-3' (aa-88, N-terminal region, 7S domain), 5'-ATTAGTGGCAGAGCTCTCG-3' (NC-1 domain), reverse: 5'-ACCCTTAGATCCGTTGCATCC-3'

Col4a4 forward: 5'-TTTGGACAGGGTACAGCTTG, reverse: 5'-TAGTGGCACACTTGGTGGAT

Col4a5 forward: 5'-CTGGAAGAATGGGTCCAGAT, reverse: 5'-GTTCCTTTGAAACCTGGGAA

Cyr61 forward: 5'-GTGAAGTGCGTCCTTGTGGACA-3', reverse: 5'-CTTGACACTGGAGCATCCTGCA-3'

EGF forward: 5'-ATCTGACTTCATGGAGACA-3', reverse: 5'-AACTGGCTCTGTCTGCCGT-3'

Egr1 forward: 5'-AGCGAACAACCCTATGAGCACC-3', reverse: 5'-ATGGGAGGCAACCGAGTCGTTT-3'

FosB forward: 5'-ACCTGTCTTCGGTGGACTCCTT-3', reverse: 5'-TGGCTGGTTGTGATTGCGGTGA-3'

GAPDH forward: 5'-CCATGGAGAAGGCTGGGG-3', reverse: 5'-CAAAGTTGTCATGGATGACC-3'

Lif forward: 5'-TCAACTGGCACAGCTCAATGGC-3', reverse: 5'-GGAAGTCTGTCATGTTAGGCGC-3'

LOX forward: 5'-CCGGTTACTTCCAGTACGGT-3', reverse: 5'-ATCCGCCCTATATGCTGAAC-3'

LOXL2 forward: 5'-GGAAAGCCTACAAGCCAGAG-3', reverse: 5'-GCAGATACCAGGTCCCACTT-3'

TNFα forward: 5'-ACGTCGTAGCAAACCACCA-3', reverse: 5'-TTGTCCCTTGAAGAAAACCT-3'

TGFβ-1 forward: 5'-CAGTGGCTGAACCAAGGAG-3', reverse: 5'-ATCCCGTTGATTCCAGGTG-3'

Vcan forward: 5'-GGACCAAGTTCCACCCTGACAT-3', reverse: 5'-CTTCACTGCAAGGTTCCTCTTCT-3'

Measurement of glomerular elasticity. Glomerular elasticity (E, Young's modulus) was measured using a microprobe indenter device(1, 2, 27). Briefly, a tensiometer probe (Kibron, Inc., Helsinki) with a 250 μm radius flat-bottom needle was mounted on a 3-D micromanipulator with 160 nm step size (Eppendorf, Inc.) attached to a Leica inverted microscope. A glass slide containing a dilute sample of glomeruli was imaged by bright field illumination, and the bottom of the probe was brought through the air-water interface until it was just above the surface of a single glomerulus (diameter ~60 μm). The probe was calibrated using the known surface tension of a pure water/air interface, and the stress applied to the probe as it was lowered onto the glomerulus was measured as a function of indentation depth. In principle, this deformation geometry is that of an infinite plane compressing a spherical object. The absolute values of elastic modulus were measured as described(27). In all cases, indentations were kept below 15 μm to avoid large strains that could damage the glomeruli. After the largest indentations, measurements were repeated at small strains to confirm that the deformations were recoverable.

Light microscopy of renal tissue. Formalin-fixed, paraffin-embedded kidney tissue was sectioned at 3 μm, and sections were stained with periodic acid-Schiff or picrosirius red stains. Stained tissue sections were examined, and digital images were collected under brightfield microscopy with an Olympus BX-80 microscope equipped with a Q-Imaging Retiga 2000R imaging system.

Immunofluorescence staining. Treated glomeruli were centrifuged at 5,000g for 5 min, resuspended and fixed in 4% paraformaldehyde for 30 minutes, and then washed 3x in PBS. Washed glomeruli were resuspended in PBS, 100 μl pipetted onto a slide, and attached to a coverslip overnight at 4˚C. The slide was rinsed in PBS and further fixed with 4% paraformaldehyde for 1 hour at room temperature. Coverslips were then washed 3x in PBS, blocked with SEA BLOCK Blocking Buffer (PIERCE) for 40 minutes, then permeabilized with 0.5% Triton X-100 in PBS for 10 minutes. Glomeruli on coverslips were stained using standard procedures, and imaging was performed using a Zeiss LSM 880 confocal microscope.

Confocal microscopy. Confocal imaging was performed in the Cell Biology and Imaging Core in the O'Brien Kidney Research Core, on a Zeiss LSM880 with Airyscan laser scanning microscope equipped with Plan-Apochromat 10x/0.3 NA, 20x/0.8 NA, 25x/0.8 NA and 63×/1.40 NA oil-immersion objective (ZEISS, Oberkochen, Germany). Fluorescence images were acquired using ZEN black 2.3 software with a 20x/0.8 NA or 63x/1.40 NA

objective and Zeiss Immersion Oil 518F was used for the 63x/1.40 NA objective. Experiments were performed at constant room temperature. Images or regions of interest (ROIs) were further processed with ZEN 2.6 (blue edition) software.

Electron microscopy. Tissue samples were fixed with 2.5% (v/v) glutaraldehyde in 0.1M sodium cacodylate buffer (pH 7.4). After three rinses with 0.1 M sodium cacodylate buffer, samples were embedded in 3% agarose and sliced into small blocks (1mm^3), rinsed with the same buffer three times and post-fixed with 1% osmium tetroxide and 0.8 % potassium ferricyanide in 0.1 M sodium cacodylate buffer for one and a half hours at room temperature. Samples were rinsed with water and then block-stained with 4% uranyl acetate in 50% ethanol for two hours. They were then dehydrated with increasing concentration of ethanol, transitioned into propylene oxide, infiltrated with Embed-812 resin, and polymerized in a 60°C oven overnight. Blocks were sectioned with a diamond knife (Diatome) on a Leica Ultracut 7 ultramicrotome (Leica Microsystems) and collected onto copper grids, post-stained with 2% aqueous uranyl acetate and lead citrate. Images were acquired on a JEM-1400 Plus transmission electron microscope equipped with a LaB_6 source operated at 120 kV using an AMT-BioSprint 16M CCD camera.

Bulk RNA sequencing. The total input of 100ng RNA was used for the library preparation on each sample. The library was prepared using Illumina TruSeq RNA Library Prep Kit v2 (RS-122-2001) according to the Manufacturer's protocol. This protocol allows RNA input of 100ng-1000ng. Illumina UMI barcodes were used to multiplex the libraries as per the Manufacturer's instructions. The quality and quantity of each sequencing final library were assessed using the Agilent 2100 BioAnalyzer system (Agilent, CA, USA). A total of 10 nM picogreen measured library was pooled for 1.3pM loading on the sequencer. The pooled libraries were sequenced on the Illumina NexSeq platform in PE75 (75 bp paired end) run with the NextSeq reagent kit v2.5 for 75 cycles. Approximately 30-40 million sequencing reads were generated per sample for the transcriptome analysis.

Paired-end demultiplexed fastq files were generated using bcl2fastq2 (Illumina, v2.17), from NextSeq550 v2.5 reagents' bcl files. Initial quality control was performed using FastQC v0.11.8 and multiqc v1.7. Fastq files were imported batch-wise, trimmed for adapter sequences, followed by quality trimming using CLC Genomics Workbench (CLC Bio, v23.0.3). The imported high-quality reads were mapped against gene regions and transcripts annotated by ENSEMBL v99 hg38 using the RNA-seq Analysis tool v2.7 (CLC Genomics

Workbench); only matches to the reverse strand of the genes were accepted (using the strand-specific reverse option). Differential gene expression analysis between the sample groups was done using the Differential Expression for RNA-seq tool v2.8, where the normalization method was set as TMM. Differential expression between the groups was tested using a control group. Outliers were downweighed, and a filter on average expression for FDR correction was enabled.

Gene expression QC, quantification, and DEG analysis. Fastq reads were aligned to the mouse genome (GENCODE Version M27), followed by a multi-step quality control process, which included assessments at the read, mapping, and dataset levels according to RNA sequencing quality control methods previously outlined (59). Gene-level expression quantification utilized HTSeq, and the resulting count data were normalized using Voom. Differential gene expression analysis was performed in R using the Limma package(60). The Benjamini & Hochberg method for controlling the false discovery rate was applied as a correction factor for the adjusted p-value. Statistically significant differentially expressed genes (DEGs) were determined based on an adjusted p-value threshold of less than 0.05. All heatmaps were created using the ComplexHeatmap R package(61).

The Podocin: Nephrin ratio (PNR), a term introduced by Roger C. Wiggins, serves as a crucial marker for assessing podocyte hypertrophic stress by examining the differential mRNA expression of Podocin (NPHS2) and Nephrin (NPHS1). Under hypertrophic stress, podocytes exhibit an increase in NPHS2 and NPHS1 mRNA, with a disproportionately higher rise in NPHS2. This ratio has been shown to correlate with podocyte density, podocyte detachment, proteinuria, progressive glomerulosclerosis, and end-stage kidney disease (ESKD)(62). Elevated PNR indicates reduced podocyte density and increased detachment, both of which contribute to proteinuria and glomerulosclerosis, ultimately progressing to ESKD. Nishizono et al. provided robust evidence supporting the association between PNR and these pathological conditions and treatment effects, underscoring its potential as a diagnostic and prognostic tool in kidney disease(63).

Identification of a TNF signature in Mouse RNAseq data. The TNF network reported in Mariani et al., 2023, which was generated from expert-curated interactions from NETPro annotations in the Genomatix Genome Analyzer database (Precigen Bioinformatics, Germany), was used to create the TNF activation score of 7-month-old mice(33). First, the mouse orthologues of the 272 genes from that paper were obtained using the ensemble biomart, yielding a TNF network of 205 mouse genes. Individual gene expression values were Z-

transformed, and group mean gene expression was calculated. The TNF activation score for each group was the average Z-score of the 205 genes.

Using human FSGS expression data at a single nuclear resolution to deconvolute 4 month old mouse RNA-seq data. We identified 77 patients from the NEPTUNE cohort with a diagnosis of FSGS. Molecular data in the form snRNA-seq was available for analysis and was utilized for this study. Using expression data from 4 month old mice a n Independent Component Analysis was performed to identify clusters of co-expressed genes in an unsupervised way. ICA is a matrix decomposition method that separates multifactorial signals into additive subcomponents. Each component could be driven by latent factors such as disease, cell type, and even noise. 25 optimal modules were extracted using Python package stabilized-ica-2.0. Optimal module number was determined as described(64). We identified one module enriched for podocyte-specific genes. Because Alport nephropathy, like FSGS, is a primary podocytopathy, we utilized this module as being reflective of podocyte injury (**Supplemental Figure S8**). Furthermore, we reasoned that because injury patterns are likely to be conserved across disease types and species, identifying the presence of these genes and their differential expression across all the time points (2, 4, and 7 months) will offer a temporal perspective on how these human data enriched podocyte genes change over time. Their alteration with TUDCA therapy will provide clues to temporal changes in these genes and therapeutic potential with TUDCA or signals downstream of TUDCA.

Author contributions

JY and ZL conducted experiments, JY, ZL, OA, and IM acquired data, JY, ZL, MA, CAA, OA, IM, SE, MK, JMH, VN, ASN, ANC, and RTM analyzed data, LAB and PAJ provided critical methods and reagents, ASN, ANC and RTM wrote the manuscript, all authors contributed to editing the manuscript.

Acknowledgments

The work published in this manuscript were supported by the National Institutes of Health grant numbers DK083592 (to LAB PAJ, and RTM), DK139111, and R56DK139111 (RTM), the Charles and Jane Pak Center for Mineral Metabolism and Clinical Research (RTM, ANC), and the NEPTUNE consortium (ASN , MK, VN, SE, MA). ASN acknowledges support of Intramural grants from the University of Michigan O'Brien Kidney Translational Core Center P30 DK081943, Taubman Institute and an extramural grant from the National Institute of Health K23 DK 125529. RTM appreciates support from the VANTHCS Research Service and COS, Jeff Hastings.

The Nephrotic Syndrome Study Network (NEPTUNE) is part of the Rare Diseases Clinical Research Network (RDCRN), which is funded by the National Institutes of Health (NIH) and led by the National Center for Advancing Translational Sciences (NCATS) through its Division of Rare Diseases Research Innovation (DRDRI). NEPTUNE is funded under grant number U54DK083912 as a collaboration between NCATS and the National Institute of Diabetes and Digestive and Kidney Diseases (NIDDK). Additional funding and/or programmatic support is provided by the University of Michigan, NephCure Kidney International, Alport Syndrome Foundation, and the Halpin Foundation. RDCRN consortia are supported by the RDCRN Data Management and Coordinating Center (DMCC), funded by NCATS and the National Institute of Neurological Disorders and Stroke (NINDS) under U2CTR002818.

References.

1. Embry AE, Mohammadi H, Niu X, Liu L, Moe B, Miller-Little WA, et al. Biochemical and Cellular Determinants of Renal Glomerular Elasticity. *PLoS One.* 2016;11(12):e0167924.

2. Embry AE, Liu Z, Henderson JM, Byfield FJ, Liu L, Yoon J, et al. Similar Biophysical Abnormalities in Glomeruli and Podocytes from Two Distinct Models. *J Am Soc Nephrol.* 2018;29(5):1501-12.

3. Liu Z, Yoon J, Wichaidit C, Jaykumar AB, Dbouk HA, Embry AE, et al. Control of Podocyte and Glomerular Capillary Wall Structure and Elasticity by WNK1 Kinase. *Front Cell Dev Biol.* 2020;8:618898.

4. Ge X, Zhang T, Yu X, Muwonge AN, Anandakrishnan N, Wong NJ, et al. LIM-Nebulette Reinforces Podocyte Structural Integrity by Linking Actin and Vimentin Filaments. *J Am Soc Nephrol.* 2020.

5. Greka A, and Mundel P. Cell Biology and pathology of podocytes. *AnnRevPhysiol.* 2012;74:299-323.

6. Hu M, Azeloglu EU, Ron A, Tran-Ba KH, Calizo RC, Tavassoly I, et al. A biomimetic gelatin-based platform elicits a pro-differentiation effect on podocytes through mechanotransduction. *Sci Rep.* 2017;7:43934.

7. Rogg M, Maier JI, Van Wymersch C, Helmstädter M, Sammarco A, Lindenmeyer M, et al. α-Parvin Defines a Specific Integrin Adhesome to Maintain the Glomerular Filtration Barrier. *J Am Soc Nephrol.* 2022.

8. Maier JI, Rogg M, Helmstädter M, Sammarco A, Schilling O, Sabass B, et al. EPB41L5 controls podocyte extracellular matrix assembly by adhesome-dependent force transmission. *Cell Rep.* 2021;34(12):108883.

9. Schell C, and Huber TB. The Evolving Complexity of the Podocyte Cytoskeleton. *J Am Soc Nephrol.* 2017;28(11):3166-74.

10. Rinschen MM, Grahammer F, Hoppe AK, Kohli P, Hagmann H, Kretz O, et al. YAP-mediated mechanotransduction determines the podocyte's response to damage. *Sci Signal.* 2017;10(474).

11. Ferrell N, Sandoval RM, Bian A, Campos-Bilderback SB, Molitoris BA, and Fissell WH. Shear stress is normalized in glomerular capillaries following 5/6 nephrectomy. *AmJPhysiol(Renal Physiol).* 2015;308:F588-F93.

12. Wyss HM, Henderson JM, Byfield FJ, Bruggeman LA, Ding Y, Huang C, et al. Biophysical properties of normal and diseased renal glomeruli. *Am J Physiol Cell Physiol.* 2011;300(3):C397-405.

13. Azeloglu EU, Hardy SV, Eungdamrong NJ, Chen Y, Jayaraman G, Chuang PY, et al. Interconnected network motifs control podocyte morphology and kidney function. *Sci Signal.* 2014;7(311):ra12.

14. Calizo RC, Bhattacharya S, van Hasselt JGC, Wei C, Wong JS, Wiener RJ, et al. Disruption of podocyte cytoskeletal biomechanics by dasatinib leads to nephrotoxicity. *Nat Commun.* 2019;10(1):2061.

15. Gyarmati G, Shroff UN, Izuhara A, Hou X, Da Sacco S, Sedrakyan S, et al. Intravital imaging reveals glomerular capillary distension and endothelial and immune cell activation early in Alport syndrome. *JCI Insight.* 2022;7(1).

16. Ding F, Wickman L, Wang SQ, Zhang Y, Wang F, Afshinnia F, et al. Accelerated podocyte detachment and progressive podocyte loss from glomeruli with age in Alport Syndrome. *Kidney Int.* 2017;92(6):1515-25.

17. Wickman L, Hodgin JB, Wang SQ, Afshinnia F, Kershaw D, and Wiggins RC. Podocyte Depletion in Thin GBM and Alport Syndrome. *PLoS One.* 2016;11(5):e0155255.

18. Schell C, Rogg M, Suhm M, Helmstädter M, Sellung D, Yasuda-Yamahara M, et al. The FERM protein EPB41L5 regulates actomyosin contractility and focal adhesion formation to maintain the kidney filtration barrier. *Proc Natl Acad Sci U S A.* 2017;114(23):E4621-e30.

19. Yu S, Gu X, Zheng Q, Liu Y, Suhas T, Du W, et al. Tauroursodeoxycholic acid ameliorates renal injury induced by COL4A3 mutation. *Kidney Int.* 2024;106(3):433-49.

20. Pieri M, Stefanou C, Zaravinos A, Erguler K, Stylianou K, Lapathitis G, et al. Evidence for activation of the unfolded protein response in collagen IV nephropathies. *J Am Soc Nephrol.* 2014;25(2):260-75.

21. Wang D, Mohammad M, Wang Y, Tan R, Murray LS, Ricardo S, et al. The Chemical Chaperone, PBA, Reduces ER Stress and Autophagy and Increases Collagen IV α5 Expression in Cultured Fibroblasts From Men With X-Linked Alport Syndrome and Missense Mutations. *Kidney Int Rep.* 2017;2(4):739-48.

22. Ioannou P, Odiatis C, Hadjisavva R, Antoniadou K, Pieri M, Malatras A, et al. Chemical chaperone 4-phenylbutyrate treatment alleviates the kidney phenotype in a mouse model of Alport syndrome with a pathogenic variant in Col4a3. *Kidney Int.* 2025.

23. Kusaczuk M. Tauroursodeoxycholate-Bile Acid with Chaperoning Activity: Molecular and Cellular Effects and Therapeutic Perspectives. *Cells.* 2019;8(12).

24. Rani S, Sreenivasaiah PK, Kim JO, Lee MY, Kang WS, Kim YS, et al. Tauroursodeoxycholic acid (TUDCA) attenuates pressure overload-induced cardiac remodeling by reducing endoplasmic reticulum stress. *PLoS One.* 2017;12(4):e0176071.

25. Panda DK, Bai X, Zhang Y, Stylianesis NA, Koromilas AE, Lipman ML, et al. SCF-SKP2 E3 ubiquitin ligase links mTORC1/ER stress/ISR with YAP activation in murine renal cystogenesis. *J Clin Invest.* 2022;132(24).

26. Uppala JK, Gani AR, and Ramaiah KVA. Chemical chaperone, TUDCA unlike PBA, mitigates protein aggregation efficiently and resists ER and non-ER stress induced HepG2 cell death. *Sci Rep.* 2017;7(1):3831.

27. Levental I, Levental KR, Klein EA, Assoian R, Miller RT, Wells RG, et al. A simple indentation device for measuring micrometer-scale tissue stiffness. *Journal of Physics: Condensed Matter.* 2010;22:191420.

28. Lake BB, Menon R, Winfree S, Hu Q, Ferreira RM, Kalhor K, et al. An atlas of healthy and injured cell states and niches in the human kidney. *Nature.* 2023;619(7970):585-94.

29. B.B. Lake RMF, J.Hansen, R. Menon, J. Basta, H. Thiessen et. al. Cellular and Spatial Drivers of Unresolved Injury and Functional Decline in the Human Kidney. *BioRxiv.* 2025.

30. Janosevic D, De Luca T, and Eadon MT. The Kidney Precision Medicine Project and Single-Cell Biology of the Injured Proximal Tubule. *Am J Pathol.* 2024.

31. P.J. McCown CB, S. Datta, V.Nair, E. Otto, D. Fermin, J. Hartman, F. Annese, F. Alakwaa, K. Latt, C. Smith, B. Godfrey, M. Larkina, A. E. Ashley-Koch, M. E. Garrett, S. Moore, K. Soldano, M. Alaba, L. H. Mariani, A. S. Naik, R. Fallegger, S. Eddy, J. Saez-Rodriguez, O. A. Olabisi, M. Kretzler. A Human Glomerular Disease Atlas defines the APOL1-JAK-STAT feed forward loop in focal segmental glomerulosclerosis. *medRxiv.* 2025.

32. Marutani T, Yamamoto A, Nagai N, Kubota H, and Nagata K. Accumulation of type IV collagen in dilated ER leads to apoptosis in Hsp47-knockout mouse embryos via induction of CHOP. *J Cell Sci.* 2004;117(Pt 24):5913-22.

33. Mariani LH, Eddy S, AlAkwaa FM, McCown PJ, Harder JL, Nair V, et al. Precision nephrology identified tumor necrosis factor activation variability in minimal change disease and focal segmental glomerulosclerosis. *Kidney Int.* 2023;103(3):565-79.

34. Abrahamson DR, Hudson BG, Stroganova L, Borza DB, and St John PL. Cellular origins of type IV collagen networks in developing glomeruli. *J Am Soc Nephrol.* 2009;20(7):1471-9.

35. Wiseman RL, Mesgarzadeh JS, and Hendershot LM. Reshaping endoplasmic reticulum quality control through the unfolded protein response. *Mol Cell.* 2022;82(8):1477-91.

36. Miner JH, and Sanes JR. Molecular and functional defects in kidneys from mice lacking collagen ‡3(IV): implications for Alport syndrome. *JCell Biol.* 1996;135(5):1403-13.

37. Andrews KL, Mudd JL, Li C, and Miner JH. Quantitative trait loci influence renal disease progression in a mouse model of Alport syndrome. *Am J Pathol.* 2002;160(2):721-30.

38. Cosgrove D, Kalluri R, Miner JH, Segal Y, and Borza DB. Choosing a mouse model to study the molecular pathobiology of Alport glomerulonephritis. *Kidney Int.* 2007;71(7):615-8.

39. Lo AC, Callaerts-Vegh Z, Nunes AF, Rodrigues CMP, and D'Hooge R. Tauroursodeoxycholic acid (TUDCA) supplementation prevents cognitive impairment and amyloid deposition in APP/PS1 mice. *Neurobiology of Disease.* 2013;50:21-9.

40. Jarad G, Knutsen RH, Mecham RP, and Miner JH. Albumin contributes to kidney disease progression in Alport syndrome. *Am J Physiol Renal Physiol.* 2016;311(1):F120-30.

41. Venkatareddy M, Wang S, Yang Y, Patel S, Wickman L, Nishizono R, et al. Estimating podocyte number and density using a single histologic section. *J Am Soc Nephrol.* 2014;25(5):1118-29.

42. Cervenka L, Mitchell KD, and Navar LG. Renal function in mice: effects of volume expansion and angiotensin II. *J Am Soc Nephrol.* 1999;10(12):2631-6.

43. Rubel D, Boulanger J, Craciun F, Xu EY, Zhang Y, Phillips L, et al. Anti-microRNA-21 Therapy on Top of ACE Inhibition Delays Renal Failure in Alport Syndrome Mouse Models. *Cells.* 2022;11(4).

44. Cortes P, Zhao X, Riser BL, and Narins RG. Regulation of glomerular volume in normal and partially nephrectomized rats. *AmJPhysiol(Renal Physiol).* 1996;270:F356-F70.

45. Wiggins JE, Goyal M, Sanden SK, Wharram BL, Shedden KA, Misek DE, et al. Podocyte hypertrophy, "adaptation," and "decompensation" associated with glomerular enlargement and glomerulosclerosis in the aging rat: prevention by calorie restriction. *J Am Soc Nephrol.* 2005;16(10):2953-66.

46. Naik AS, Wang SQ, Chowdhury M, Aqeel J, O'Connor CL, Wiggins JE, et al. Critical timing of ACEi initiation prevents compensatory glomerular hypertrophy in the remaining single kidney. *Sci Rep.* 2021;11(1):19605.

47. Kashtan CE, and Gross O. Clinical practice recommendations for the diagnosis and management of Alport syndrome in children, adolescents, and young adults-an update for 2020. *Pediatr Nephrol.* 2021;36(3):711-9.

48. Desjardins M, and Bendayan M. Ontogenesis of glomerular basement membrane: structural and functional properties. *J Cell Biol.* 1991;113(3):689-700.

49. Rheault MN, Kren SM, Thielen BK, Mesa HA, Crosson JT, Thomas W, et al. Mouse model of X-linked Alport syndrome. *JASN.* 2004;15:1466-74.

50. Gale DP, Gross O, Wang F, Esteban de la Rosa RJ, Hall M, Sayer JA, et al. A Randomized Controlled Clinical Trial Testing Effects of Lademirsen on Kidney Function Decline in Adults with Alport Syndrome. *Clin J Am Soc Nephrol.* 2024;19(8):995-1004.

51. Widjaja AA, Shekeran SG, Adami E, Ting JGW, Tan J, Viswanathan S, et al. A Neutralizing IL-11 Antibody Improves Renal Function and Increases Lifespan in a Mouse Model of Alport Syndrome. *J Am Soc Nephrol.* 2022.

52. Keestra-Gounder AM, Byndloss MX, Seyffert N, Young BM, Chávez-Arroyo A, Tsai AY, et al. NOD1 and NOD2 signalling links ER stress with inflammation. *Nature.* 2016;532(7599):394-7.

53. Wang W, Zhao J, Gui W, Sun D, Dai H, Xiao L, et al. Tauroursodeoxycholic acid inhibits intestinal inflammation and barrier disruption in mice with non-alcoholic fatty liver disease. *Br J Pharmacol.* 2018;175(3):469-84.

54. Groopman EE, Marasa M, Cameron-Christie S, Petrovski S, Aggarwal VS, Milo-Rasouly H, et al. Diagnostic Utility of Exome Sequencing for Kidney Disease. *N Engl J Med.* 2019;380(2):142-51.

55. Deltas C, Savva I, Voskarides K, Papazachariou L, and Pierides A. Carriers of Autosomal Recessive Alport Syndrome with Thin Basement Membrane Nephropathy Presenting as Focal Segmental Glomerulosclerosis in Later Life. *Nephron.* 2015;130(4):271-80.

56. Schlondorff D. Preparation and study of isolated glomeruli. *Methods in Enzymology.* 1990;191:130-40.

57. Naldini L, Blömer U, Gallay P, Ory D, Mulligan R, Gage FH, et al. In vivo gene delivery and stable transduction of nondividing cells by a lentiviral vector. *Science.* 1996;272(5259):263-7.

58. Shankland SJ, Pippin JW, Reiser J, and Mundel P. Podocytes in culture: past, present, and future. *Kidney International.* 2007;72(1):26-36.

59. Hong C, Eichinger F, Atta MG, Estrella MM, Fine DM, Ross MJ, et al. Viral associations with kidney disease diagnosis and altered kidney metatranscriptome by kidney function. *Kidney Int.* 2023;103(1):218-22.

60. Ritchie ME, Phipson B, Wu D, Hu Y, Law CW, Shi W, et al. limma powers differential expression analyses for RNA-sequencing and microarray studies. *Nucleic Acids Res.* 2015;43(7):e47.

61. Gu Z. Complex heatmap visualization. *Imeta.* 2022;1(3):e43.

62. Fukuda A, Wickman LT, Venkatareddy MP, Wang SQ, Chowdhury MA, Wiggins JE, et al. Urine podocin:nephrin mRNA ratio (PNR) as a podocyte stress biomarker. *Nephrol Dial Transplant.* 2012;27(11):4079-87.

63. Nishizono R, Kikuchi M, Wang SQ, Chowdhury M, Nair V, Hartman J, et al. FSGS as an Adaptive Response to Growth-Induced Podocyte Stress. *J Am Soc Nephrol.* 2017;28(10):2931-45.

64. Kairov U, Cantini L, Greco A, Molkenov A, Czerwinska U, Barillot E, et al. Determining the optimal number of independent components for reproducible transcriptomic data analysis. *BMC Genomics.* 2017;18(1):712.

Figures.

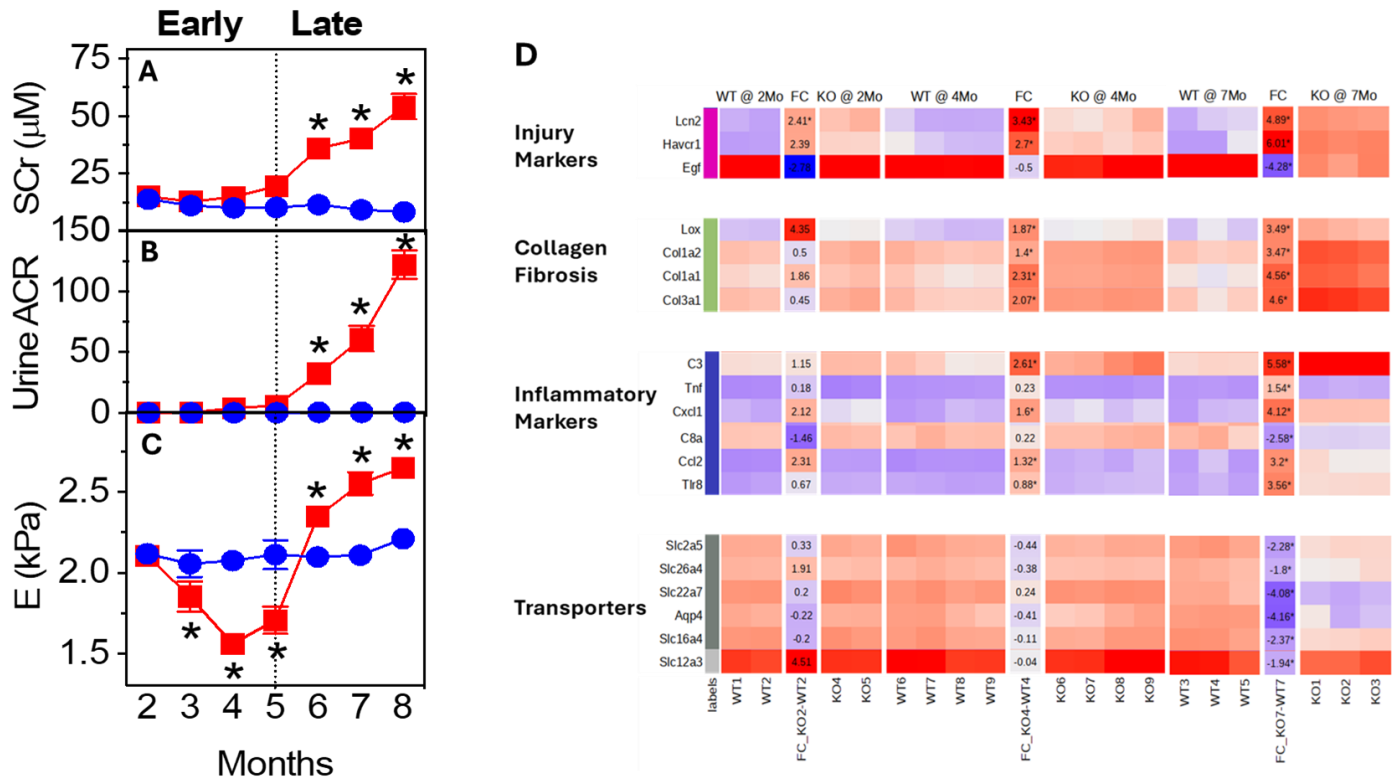

Figure 1. Measurement of SCr (**A**), urine ACR (**B**), and glomerular elastic modulus (E, Young's modulus) (**C**) in Control (Blue) and *Col4α3*$^{-/-}$ (KO, red) mice over the course of renal disease compared to wildtype or heterozygote controls. Beginning two months after birth, SCr (μM) and urine ACR (mg/g) were measured monthly through eight months. Glomerular E (kPa) was measured in mice sacrificed at the indicated time point using microindentation of isolated glomeruli. Each point in the graphs shows average E values from 4 - 12 different mice with 6 – 10 glomeruli measured in each mouse. Significance was determined by 2-way ANOVA using Graphpad; **P<0.01, ****P<0.0001. **(D)** Differentially expressed genes in *Col4α3*$^{-/-}$ kidneys at 2, 4, and 7 months compared to age-matched WT. N=2 per group at 2 months, 4 per group at 4 months, and 3 per group at 7 months. Each column represents an individual mouse.

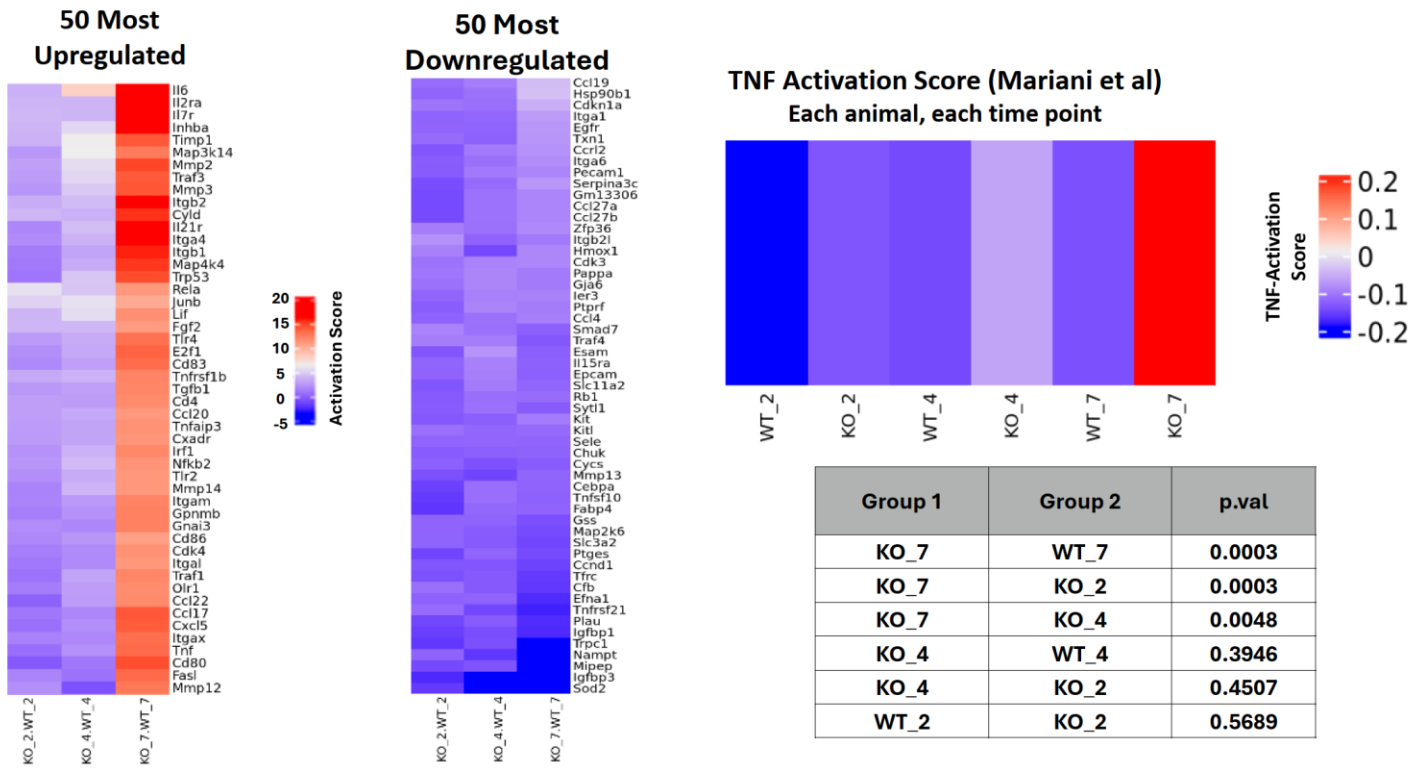

Group 1	Group 2	p.val
KO_7	WT_7	0.0003
KO_7	KO_2	0.0003
KO_7	KO_4	0.0048
KO_4	WT_4	0.3946
KO_4	KO_2	0.4507
WT_2	KO_2	0.5689

Figure 2. Genes and Gene Products Activated by TNF in Col4α3$^{-/-}$ Mice Compared to NEPTUNE FSGS/MCD database. RNAseq data from WT and *Col4α3*$^{-/-}$ mice were analyzed for TNF signaling using the human 272 gene TNF network from Mariani et al(30). Mouse orthologs (205) of the 272-gene human TNF signature were identified. Individual gene expression values for each mouse were Z-transformed, and group mean gene expression was calculated. A) heatmaps showing the 50 most upregulated and 50 most downregulated genes. Each column corresponds to comparison of WT and *Col4α3*$^{-/-}$ mice at each time point (2 Mo - 2 mice WT and *Col4α3*$^{-/-}$; 4 Mo – 4 mice WT and *Col4α3*$^{-/-}$; 7 Mo – 3 mice WT and *Col4α3*$^{-/-}$. The TNF activation score for each group of mice was the average Z-score of the 205 genes. B) Heatmap showing WT, *Col4α3*$^{-/-}$, 2 – 7 Mo with significance of comparisons below.

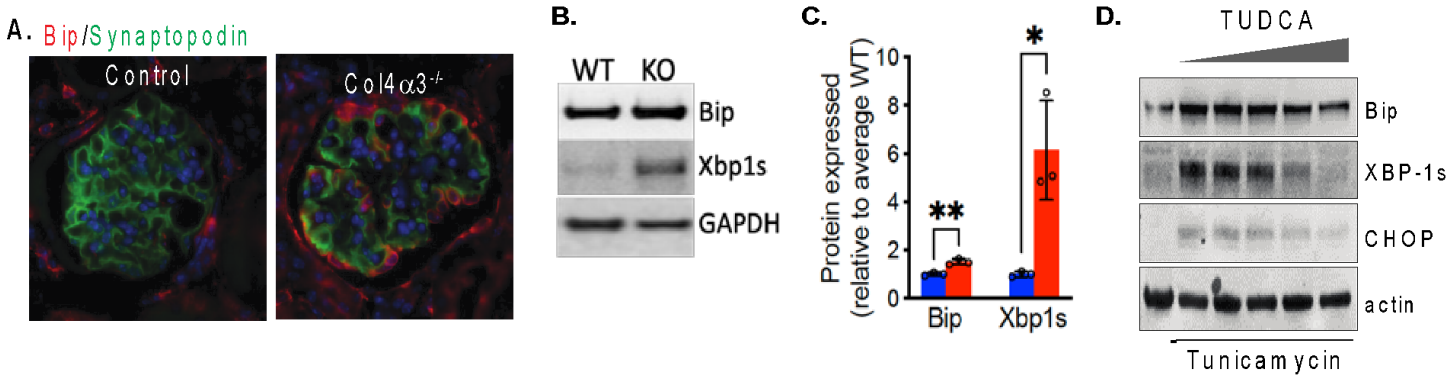

Figure 3. Evidence of UPR activation in glomeruli and podocytes from *Col4α3*$^{-/-}$ mice. A) Immunofluorescence images of Bip and Synaptopodin staining in 4-month WT and *Col4α3*$^{-/-}$ mouse glomeruli, **B)** Blots of UPR markers in podocyte cell lines under basal conditions derived from WT and *Col4α3*$^{-/-}$ (KO) mice. The cells were maintained under standard conditions, harvested in RIPA buffer at 7% confluence, and the crude extract was immunoblotted with antibodies against Bip, Xbp1s, and GAPDH. The conditionally immortalized WT and *Col4α3*$^{-/-}$ cells were developed from primary cultures of 3-month WT and Col4α3$^{-/-}$ glomeruli. **C)** Comparison of Bip and Xbp1s protein expression from B (N=3, normalized to WT). **D)** Efficacy of TUDCA for blocking tunicamycin-induction of UPR marker expression in WT podocytes. Podocytes were treated with tunicamycin 1 µg/ml and then increasing concentrations of TUDCA from 1 - 4 mM for four hours.

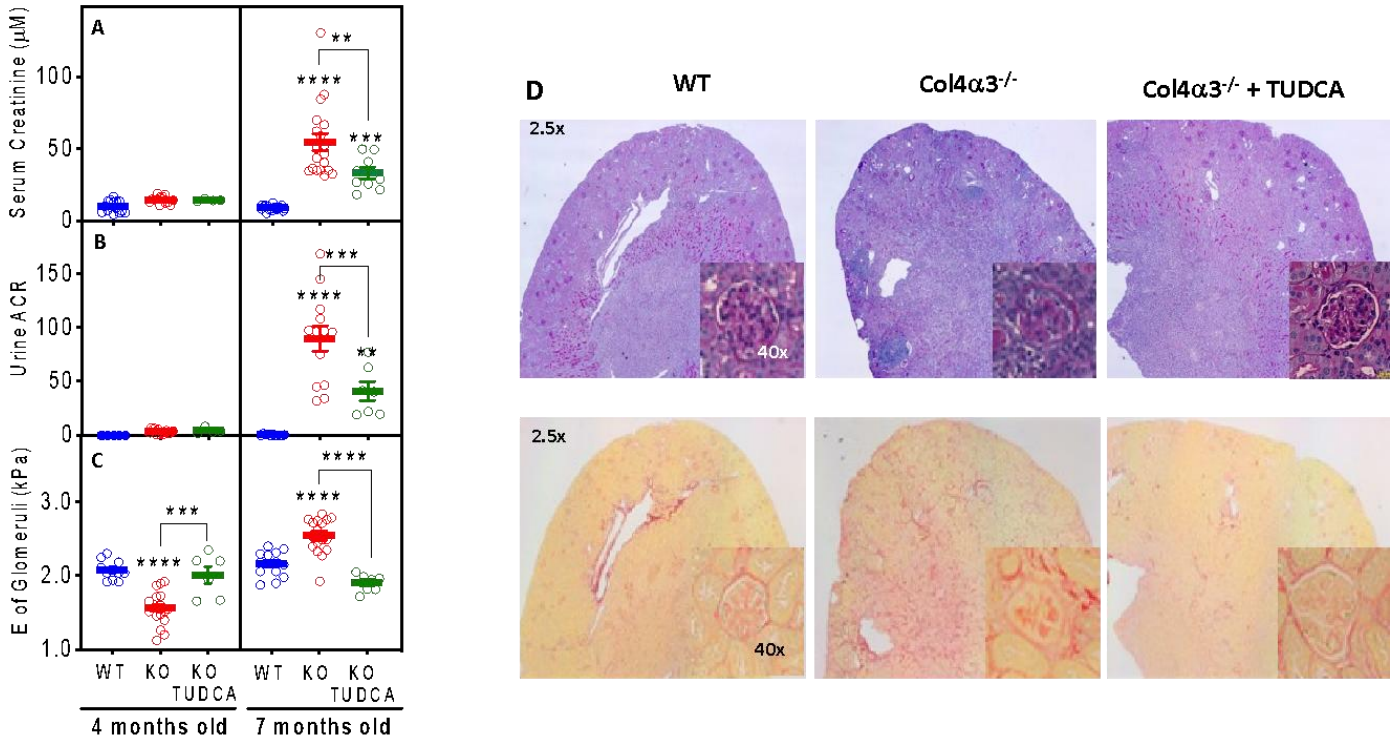

Figure 4. TUDCA treatment slows the progression of renal disease and minimizes changes in E in Col4α3$^{-/-}$ mice. Col4α3$^{-/-}$ (KO) mice were treated from weaning (approximately 4 weeks) with 0.8% TUDCA mouse chow (KO TUDCA) until sacrifice. At 4 and 7 months of age, SCr (µM) (**2A**), urine ACR (**2B**), and glomerular elastic modulus (E, kPa) (**2C**) was measured in WT (Blue), KO (Red) and TUDCA-treated KO animals (Green). In A and B, each circle represents a measurement from one mouse, and in C, each circle represents E measured from an average of 6-10 individual glomeruli from a single mouse. Significance was determined by ANOVA and multiple comparisons test using GraphPad; **P<0.01, ***P<0.001, ****P<0.0001. **2D.** Comparison of kidney cortex from WT, *Col4α3$^{-/-}$* (KO), and TUDCA treated *Col4α3$^{-/-}$* (KO) animals. Top row, sections from 7-month mice are stained with PAS and bottom row sections from 7-month mice are stained with picrosirius red. Insets in each panel show representative glomeruli from each condition.

Fibrosis	WT (N)	KO (N)	KO-TUDCA (N)
Col1α1	1 (4)	55.5 ± 13 (3)	26.2± 6.2 (4)
Col1α2	1 (4)	29.6 ± 7.3 (5)	13.9 ± 3.2 (4)
Col3α1	1 (4)	74.1 ± 31.9 (5)	31.9 ± 2.4 (4)
Lox	1 (4)	29.7 ± 7.4 (3)	13..3 ± 7.6 (4)
Loxl2	1 (4)	21.5 ± 7.1 (3)	6.7 ± 3.1 (4)
Cytokines			
TGF-β1	1 (4)	4.8 ± 0.8 (4)	3.0 ± 0.7 (4)
TNF-α	1 (4)	30.3 ± 7.9 (3)	14.3 ± 3.0 (4)
IGF-1	1 (4)	9.81 ± 2.23 (4)	5.93 ± 1.72 (4)
Chemokines/Receptors			
Cxcl1	1 (4)	45.0 ± 11.4 (4)	20.9 ± 2.11 (3)
Ccl2	1 (4)	41.5 ± 9.3 (4)	34.6 ± 5.68 (4)
Ccr2	1 (4)	15.0 ± 3.45 (5)	4.04 ± 1.57 (3)
Injury Markers			
EGF	1 (4)	0.20 ± 0.1 (5)	0.7 ± 0.2 (4)
Ccn1 (Cyr61)	1 (4)	4.46 ± 0.6 (3)	2.0 ± 1.0 (4)

Table 1. Summary of qRT-PCR of selected fibrosis, cytokine, chemokine, or injury-related genes in 7-month *Col4α3*$^{-/-}$ mice without (KO) and with (KO-TUDCA) TUDCA treatment, compared to age-matched WT littermates. All values in KO and KO-TUDCA groups represent fold change from 4-month-old WT ± SD as determined by ANOVA. The number of samples in each group is shown in parentheses after the values (N).

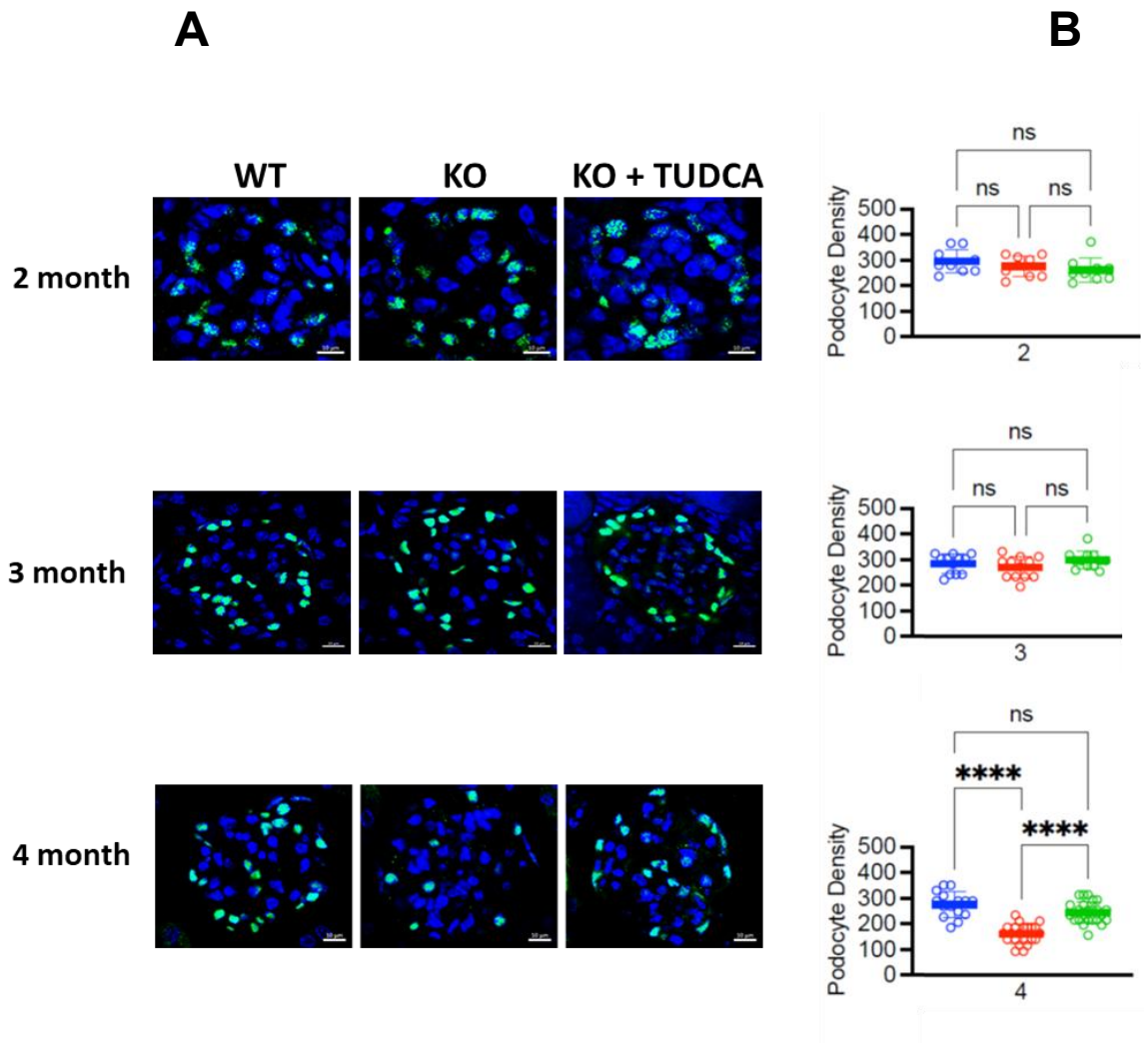

Figure 5. TUDCA reduces podocyte loss from *Col4α3*$^{-/-}$ mouse glomeruli. A) Representative glomeruli in kidney sections from WT, *Col4α3*$^{-/-}$ (KO), and TUDCA-treated *Col4α3*$^{-/-}$ (KO+TUDCA) mice from 2, 3, and 4- 4-month-old mice were stained for WT-1 and DAPI. Scale bar: 10 μm. **B)** Summary of podocyte density analysis. WT – Blue, *Col4α3*$^{-/-}$ - Red, and *Col4α3*$^{-/-}$ + TUDCA Green. The number of WT-1 and DAPI-positive nuclei in 20 glomeruli from 3 mice was counted and used for podocyte density calculations. Each dot represents the number of WT-1 positive nuclei in a single glomerulus. Data are shown as mean ± SEM and significance was determined by ordinary one-way ANOVA, followed by Dunnett's multiple comparisons test, ****P<0.0001. At 2 months - Podocytes/10^6 μm^3 ± SD, WT 296±44, *Col4α3*$^{-/-}$ 276±39, and *Col4α3*$^{-/-}$+TUDCA 262±45). At 3 months - Podocytes/10^6 μm^3 ± SD, WT 285±35, *Col4α3*$^{-/-}$ 270±40, and *Col4α3*$^{-/-}$+T 299±32). At 4 months, Podocytes/10^6 μm^3 ± SD, WT 276±48, *Col4α3*$^{-/-}$ 162±37, and *Col4α3*$^{-/-}$+TUDCA 246±40).

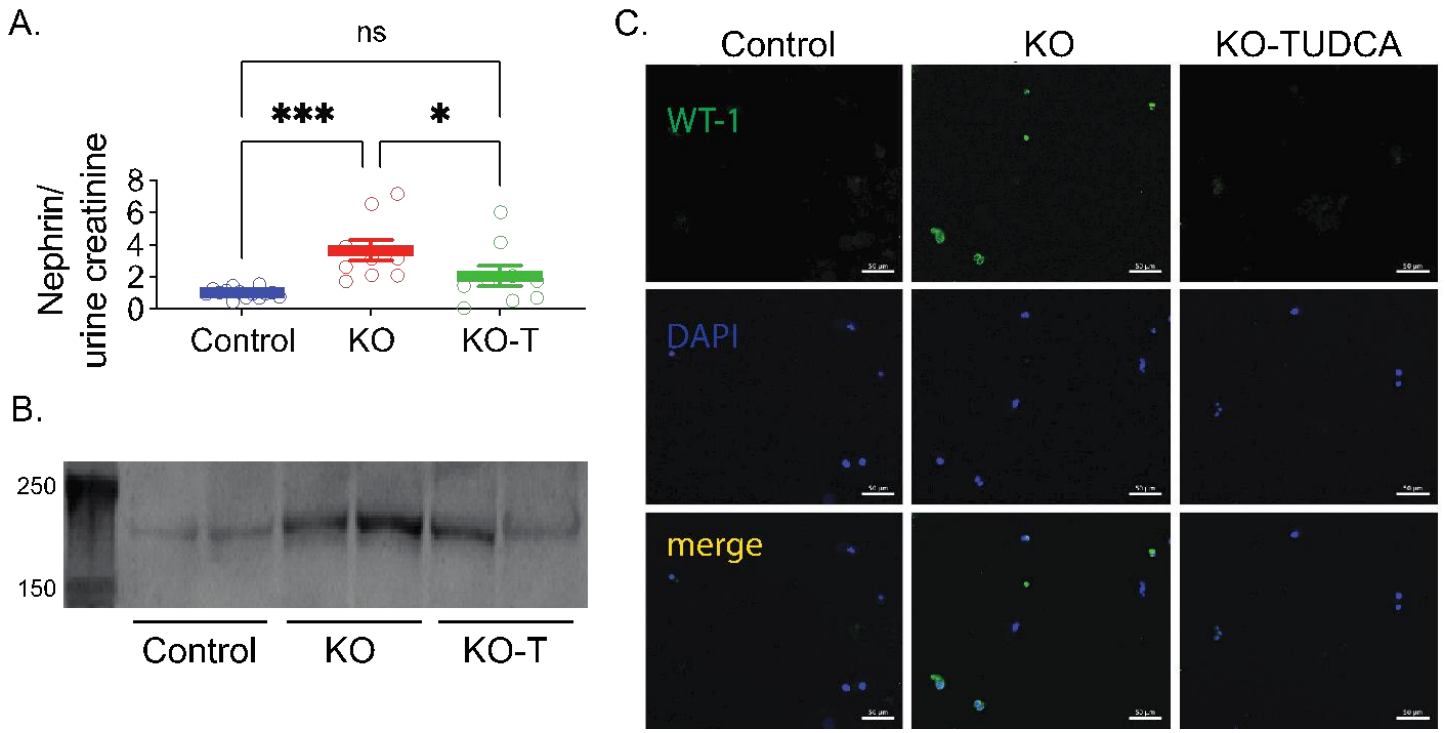

Figure 6. Glomerular capillary deformability and podocyte adhesion. WT (Control), *Col4α3*$^{-/-}$ (KO), and *Col4α3*$^{-/-}$ + TUDCA (KO-TUDCA) mice were injected (IP) with 0.5N saline (80 µl/g IP), and urine was collected over the subsequent two hours. The urine samples were normalized for creatinine, immunoblotted for nephrin, and quantified with densitometry. The urine pellet was stained for WT-1 and DAPI. **A**) shows aggregate data for all sample groups expressed as nephrin/creatinine (arbitrary densitometry units for nephrin) for each sample group. WT – Blue, *Col4α3*$^{-/-}$ - Red, and *Col4α3*$^{-/-}$ + TUDCA Green. Each point represents a sample from a single mouse; the bar indicates mean ± SEM. Significance was determined by ordinary one-way ANOVA, followed by Tukey's multiple comparisons test; *P<0.05, ***P<0.001. **B**) Representative urine nephrin immunoblot with duplicate samples, loading normalized with creatinine. **C**) Representative urine sediment samples stained for WT-1 and DAPI.

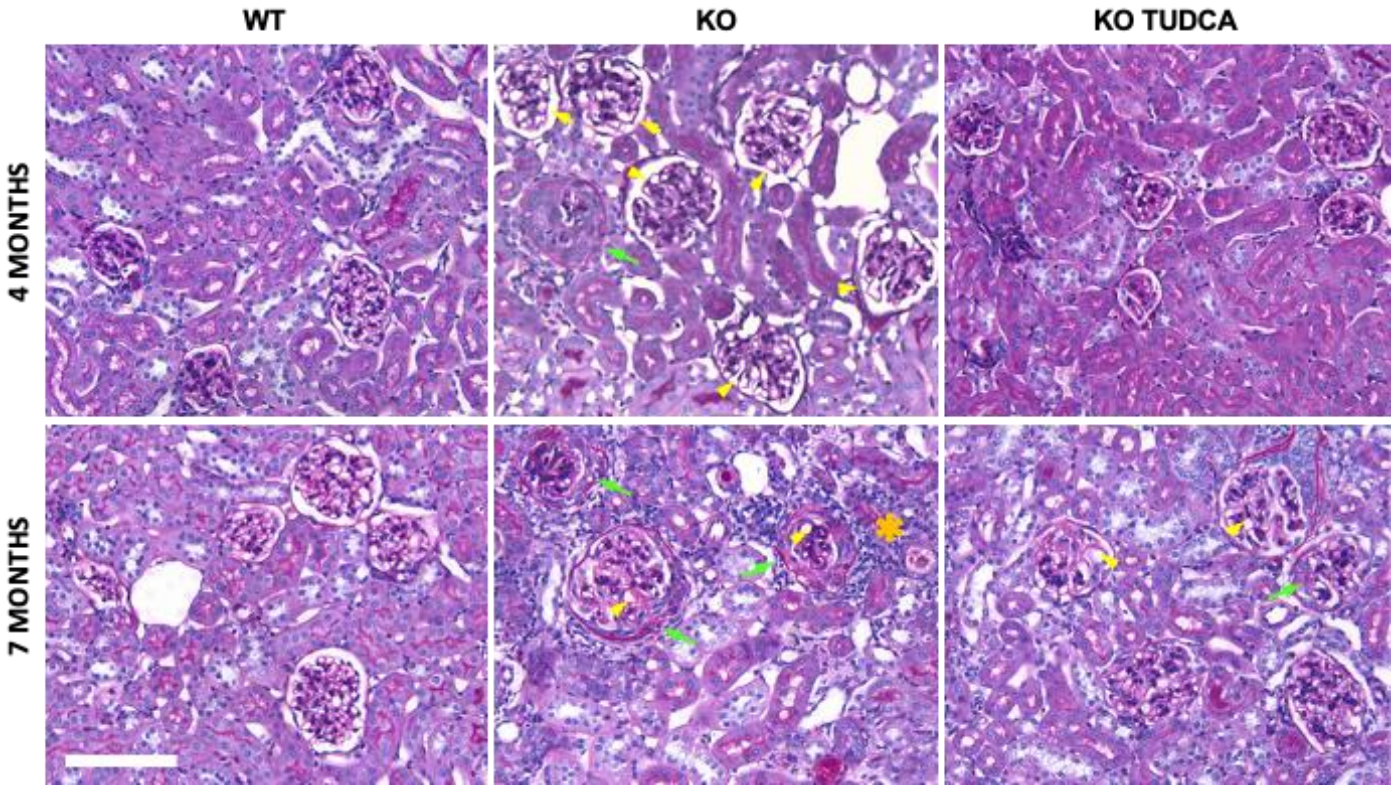

Figure 7. Photomicrographs of PAS-stained kidney sections from 4-month-old (top row) and 7-month-old (bottom row) WT, *Col4α3*$^{-/-}$ (KO), and TUDCA-treated *Col4α3*$^{-/-}$ (KO TUDCA) mice. The 4-month KO image shows glomerular enlargement, focal proliferative glomerular lesions (green arrow), and dilation of glomerular capillary lumens (yellow arrowheads) that are not observed in Control (top left) or the TUDCA-treated KO mice (top right). The 7-month KO mice (bottom center) show more extensive glomerular proliferative lesion development (green arrows), with proliferation composed predominantly of epithelial cells filling Bowman's space, along with patchy areas of tubular atrophy and interstitial fibrosis and chronic inflammation (orange asterisk). The section from the 7-month TUDCA-treated mice shows evidence of less severe glomerular injury. Scale bar = 200 μm for all images.

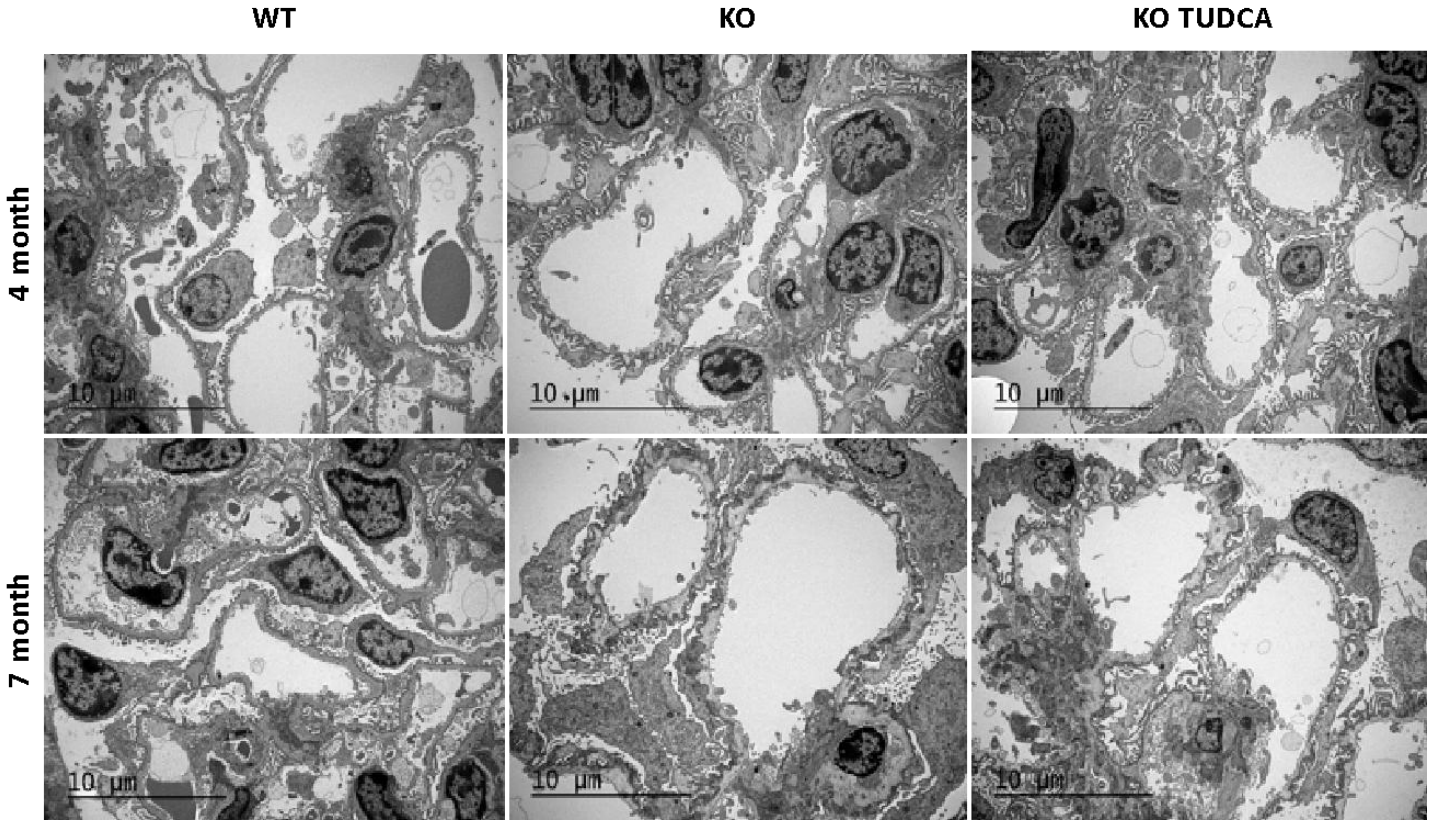

Figure 8. Transmission Electron micrographs of mouse kidneys, showing glomerular changes at 4 (top row) and 7 (bottom row) months in WT, *Col4α3*$^{-/-}$ (KO), and TUDCA-treated *Col4α3*$^{-/-}$ (KO TUDCA) mice. At 4 months, glomeruli of KO mice (top center) and KO TUDCA mice (top right) reveal features of segmental podocyte injury, including mild segmental podocyte foot process effacement, more extensive but segmental foot process irregularity, and mild microvillous change. These podocyte changes are concurrent with segmentally prominent "knob-like" subepithelial basement redundancy, characteristic of the *Col4α3*$^{-/-}$ mouse model. WT mice (top left) show none of these changes. TUDCA treatment reduces the severity and extent of glomerular pathology. At 7 months (bottom row), KO mice (bottom center) reveal more severe and widespread podocyte injury, demonstrated by extensive podocyte foot process effacement and irregularity, cellular hypertrophy, and microvillous change. There are also comparable glomerular basement membrane changes including extensive subepithelial basement redundancy and segmental "basket weave", and segmental glomerular capillary loop dilation. In contrast, 7-month KO TUDCA mice (bottom right) show podocyte and glomerular basement membrane changes that are similar in nature to those of the KO mice but are less extensive and more segmental. None of these changes are seen in WT mice (bottom left). All images are the same magnification – scale bar = 10 µm.